

# Magnetotelluric images of the medium enthalpy Bakreswar geothermal province within a granitic gneissic complex, Eastern Indian Peninsula

Roshan K. Singh<sup>1,2,3</sup>  | Ute Weckmann<sup>2</sup> | Shalivahan Srivastava<sup>1,3</sup> 

<sup>1</sup>Indian Institute of Technology (ISM), Dhanbad, India

<sup>2</sup>GFZ, German Research Centre for Geosciences, Potsdam, Germany

<sup>3</sup>Indian Institute of Petroleum & Energy, Visakhapatnam, India

## Correspondence

Roshan K. Singh, Indian Institute of Technology (ISM), Dhanbad, India.  
Email: roshanmanjitsingh@gmail.com

## Funding information

Deutscher Akademischer Austauschdienst (DAAD)

## Abstract

The Bakreswar geothermal province represents a medium enthalpy geothermal system with its Bakreswar and Tantloie hot springs. It lies within the Chotanagpur Granite Gneissic Complex in the eastern part of the Indian Peninsula. The province has a high heat flow and a high geothermal gradient of 90°C/km. Magnetotelluric data from 95 sites in a frequency range of 10 kHz–10 Hz were acquired over the Bakreswar geothermal province to obtain an electrical conductivity model and map the geothermal reservoir with its fluid pathways and related geological structures. Subsurface conductivity models obtained from three-dimensional inversions of the Magnetotelluric data exhibit several prominent anomalies, which are supplemented by gravity results. The conductivity model maps three features which act as a conduit (a) a northwest–southeast trending feature, (b) an east–west trending feature to the south of the northwest–southeast trending feature (which lies 1 km north of the Oil and Natural Gas Corporation fault marked by previous studies) and (c) shallow conducting features close to Bakreswar hot spring. The northwest–southeast trending feature coincides with the boundary of the high-density intrusive block. This northwest–southeast trending feature provides the pathway for the meteoric water to reach a maximum depth of 2.7 km, where it gets heated by interacting with deep-seated structures and then it rises towards the surface. The radiogenic process occurring within the granites of Chotanagpur Granite Gneissic Complex provides the heat responsible for heating the meteoric water. The northwest–southeast and east–west trending features are responsible for the transport of meteoric water to deeper depths and then towards the shallow regions of the Earth. The near surface features close to the Bakreswar hot spring are responsible for carrying the water further towards the hot spring. The resistivity of these structures plotted as a function of salinity and temperatures for saline crustal fluids suggests the involvement of meteoric water. Further, applying Archie's law to this resistivity suggests that the conduit path has a porosity greater than 10%. This study successfully maps the anomalous structures which might foster the migration of geothermal fluid in Bakreswar geothermal province.

This is an open access article under the terms of the Creative Commons Attribution-NonCommercial-NoDerivs License, which permits use and distribution in any medium, provided the original work is properly cited, the use is non-commercial and no modifications or adaptations are made.

© 2023 The Authors. *Geophysical Prospecting* published by John Wiley & Sons Ltd on behalf of European Association of Geoscientists & Engineers.



## KEYWORDS

electromagnetics, geothermal, gravity, inversion, magnetotellurics, modelling

## INTRODUCTION

Geothermal regions are important because of their ability to store natural heat in the rocks and fluids within the Earth subsurface. A geothermal system can be defined as geological setting where the part of Earth's thermal energy may be extracted from natural or artificially induced circulating fluids and transported to the point of application (Williams et al., 2011; Neuendorf et al., 2005; Moeck, 2014). The surface manifestations of geothermal energy are volcanoes, fumaroles, geysers, steaming grounds and hot springs. The basic components of a geothermal system are a heat source, fluids (which also act as carrier of heat in the system), a fluid reservoir and a fluid conduit. The productivity of geothermal system is controlled by three primary factors that interact dynamically. These factors comprise the heat source(s) and Earth's crustal heat flow; permeability of faults, fracture networks and geological formations; and the patterns of fluid flow. These factors depend largely on plate tectonics event in the region, and therefore, a comprehensive understanding of plate tectonics is critical for understanding the geothermal setting of the area (Moeck, 2014). The radioactive decay of elements – mainly Uranium, Thorium and Potassium – in Earth's mantle and crust results in heat energy as a by-product. For example, heat generated within the granite in White Mountains in New Hampshire (Birch et al., 1968), Cooper Basin, Australia, northern Illinois (Roy et al., 1989) and the Gonghe basin, on the Northeastern Tibetan plateau (Zhang et al., 2020). Fluids play an important role in geothermal system utilization, as they are necessary for transporting heat from the reservoir to the surface. The volume of produced fluids determines whether a geothermal play system is economic/economical. Often meteoric water constitutes the fluid in high temperature dominated geothermal system where the meteoric water after being heated at depth rises towards the surface again to mix with groundwater and drain out from hot springs (Meju, 2002). Examples for such an environment may be liquid-dominated geothermal systems, for example, associated with the Taupo Volcanic Zone in New Zealand (Bibby et al., 1995).

In general, the geothermal systems are subsumed in different types according to the temperature and/or the nature and properties of the reservoir. A key property to distinguish geothermal systems is related to the emplacement of magma. Magmatic geothermal systems cover convective hydrothermal, hot dry rock and partial melt systems, whereas hot fluids in sedimentary or crystalline reservoirs are described as non-volcanic resources (Meju, 2002). In terms of heat source,

many active geothermal provinces are termed amagmatic as no magmatic intrusions are observed in the upper crust (Roche et al., 2019; Hacıoğlu et al., 2020).

Amagmatic/non-magmatic geothermal system shows large variations in its geometry making it difficult to develop its conceptual model (Munoz et al., 2014). In these systems, mapping the distribution of electrical conductivity helps in the identification of deep aquifers which can act as reservoirs and pathways for fluids. The Lluçmajor aquifer system in southern Mallorca Island, Spain (Arango et al., 2009), and Groß Schoenebeck geothermal system North of Berlin, Germany (Munoz et al., 2010), are examples of non-volcanic geothermal system.

A prospective geothermal system is influenced by a convection or conduction mode of heat transfer. The convection-dominated geothermal systems due to their fluid dynamics are often mentioned as feasible or active geothermal systems. These systems host high enthalpy resources and are situated at plate tectonic margins, or settings of active tectonism or volcanism.

The conduction-dominated geothermal systems host low-to-medium enthalpy resources and are referred to as passive geothermal systems because fast convective flows of fluids are absent and less short-term fluid dynamics. These systems are situated mainly at passive tectonic plate settings with no occurrence of major tectonic or volcanic activity. An important factor in understanding the occurrence of convection and conduction-dominated play systems is distinguishing between igneous and amagmatic geothermal plays. Conduction-dominated systems in or close to igneous rocks are related to high radiogenic heat production (typically high heat-producing element-rich granites), but no active volcanism and minor or no active tectonism. A convection-dominated magmatic system has a magma chamber as the source of heat and these systems are located in volcanic and tectonically active areas.

Moeck (2014) prepared a catalogue of prospective geothermal system and mentioned that the geologic controls in conduction-dominated geothermal are either litho or biofacies of sedimentary rock and faults and fractures. The plate tectonic settings in these systems are constituted by intracontinental intrusion in a flat terrain. The granite rocks with high radiogenic heat production are host rocks in these systems. In these geothermal settings, the systems of faults and fractures act as channels (conduits) for the geothermal fluids to travel from deeper crustal levels to shallow levels where they are tapped by the geothermal wells to produce power (Curewitz & Karson, 1997; Jolie et al., 2021). Faults

are the permeable structures which primarily control the pattern of fluid flow, with most up-flow zones existing in complex fault interaction zones.

Jolie et al. (2021) presented the favourable structural settings for the exploitation of geothermal systems and mentioned that most intermediate-temperature ( $\geq 125^{\circ}\text{C}$ ) to high geothermal system ( $\geq 225^{\circ}\text{C}$ ) are located along normal faults in complex interaction zones, such as (a) termination of faults, (b) fault interactions of fault, (c) step overs or relay ramps, accommodation zones, (d) displacement transfer zones and (e) releasing bends or pull aparts (example include Taupo Volcanic zone of New Zealand). Robust geothermal systems flourish in complex structural settings that possess multiple types of favourable structures (Faulds et al., 2013), for example geothermal systems in the Basin and Range Province of Western USA (such as Steamboat and McGinness Hills) which incorporates multiple fault termination (Faulds & Stewart, 1998) and in the Taupo-Volcanic Zone of New Zealand (including Ohaaki-Broadlands and Wairakei; Rowland & Simmons, 2012).

Patro (2017) discussed geothermal resources in Asia and the application of the magnetotelluric (MT) method for their exploration which included for instance the Hailin Geothermal Anomaly, in Mudanjiang, China, the Lahendong and Kamojang Geothermal Systems in Indonesia. On the basis of enthalpy and temperature classifications (Benderitter & Cormy, 1990), the majority of Indian geothermal systems can be classified as medium enthalpy ( $100\text{--}200^{\circ}\text{C}$ ) geothermal system (Razdan et al., 2008). Based on tectonic elements and heat flows/geothermal gradients measured from the thermal springs in the region, the geothermal regions in India have been categorized as the Himalayan province, Sohana province, West coast province, Gujarat-Rajasthan province, Godavari province, Mahanadi province, and Son-Narmada-Tapti (SONATA) (SONATA is a fault-bounded rift zone which extends in east-west direction through the central part of India. This structural feature hosts several thermal springs which constitute the 'SONATA geothermal province' (GSI, 1991; Majumdar, 2009; Singh et al., 2015)) geothermal province (Singh et al., 2016).

Electrical conductivity increases with the concentrations of dissolved salts in the geothermal fluids (Munoz, 2014) and the temperature; thus, it is an important physical parameter for the characterization of a geothermal system. The MT method is particularly useful for mapping the electrical conductivity of the subsurface. In a geothermal setting, it can be used for structural investigations to map anomalous conductive zones and to identify the conduit path of fluids (e.g. Amatyakul et al., 2015; Bai et al., 2001; Bhattacharya et al., 2002; Hariharayana et al., 2006; Meju, 2002; Munoz et al., 2010; Oskooi et al., 2005; Sinharay et al., 2010; Uchida et al., 2004, 2005; Volpi et al., 2003; Wannamaker et al., 2004).

The Bakreswar geothermal system with a reservoir temperature of  $120\text{--}140^{\circ}\text{C}$  is a medium enthalpy geothermal system (Gupta et al., 2015; Singh et al., 2016; Sarolkar, 2018). It is situated at the easternmost end of the fault-bounded SONATA rift zone. The Bakreswar geothermal province (BGP) is located within the Chotanagpur Granite Gneissic Complex (CGGC) in the eastern part of the Indian Peninsula (Figure 1). The gas discharge from the Bakreswar geothermal area shows a very high concentration of helium and very low ratios of Kr/Xe which indicates the effect of radiogenic processes taking place (Majumdar et al., 2009). The granites of the CGGC host Uranium mineralizations (Ghose & Chatterjee, 2008; Sarangi, 2003), which are causative for the radiogenic heat in the area; similar to the granites in the Guangdong province, Southern China (Sun et al., 2015) and granites of the Cenozoic Mourne Mountains, early Caledonian Carnsore Granite and late Caledonian Costelloe Murvey Granite in Ireland (Noller et al., 2015). All authors implied regarding the heat source that the granites hosting uranium mineralizations provide the radiogenic heat and have the potential of a geothermal resource. The main hot springs in the BGP are Bakreswar (BHS) and Tantloie hot springs (THS), which are approximately 20 km apart (Figure 1). The heat flow in the BGP is very high with values varying from 145 to  $180\text{ mW/m}^2$  (Shanker, 1988; Chandrasekharam, 2000), and therefore it can be used for both power generation and direct use of heat (Tester et al., 2005). The high level of discharge of helium in BHS indicates the deep source of thermal energy (Chaudhuri et al., 2010). Levels of  $\delta^{18}\text{O}$  and  $\delta\text{D}$  in the spring water from BHS and THS and the local ground water indicate that the geothermal fluids are of meteoric origin, and these springs are related genetically (Majumdar et al., 2005). The geothermal gradient in the area is  $90^{\circ}\text{C/km}$  (Shanker et al., 1988; Chandrasekharam, 2000), which makes it economically feasible and valuable to drill down to a depth of 5 km (Goldstein et al., 2011). The previous geophysical studies conducted in close vicinity of the BHS include self-potential, gravity, magnetic, electrical resistivity and audio MTs surveys (Bhattacharya et al., 1992; Mukhopadhyay, 1996; Majumdar et al., 2000; Roy et al., 1985; Sinharay et al., 2010), and these studies have been unable to map the reservoir and/or the major fluid conduit. Sinharay et al. (2010) suggested that the reservoir of BHS is probably located towards the west of the hot spring. In this paper, we present MT results obtained from the area, in order to (a) characterize the area between two hot springs, namely BHS and THS, (b) delineate the geothermal reservoir, (c) map possible pathways of hot fluid and (d) establish the relationship among the various geological boundaries present in the south-west of the study area. We further analysed and interpreted the resistivity value of the conduit path to understand the nature of the geothermal fluid, the temperature of the fluid in the anomalous structures, and the porosity of these structures.

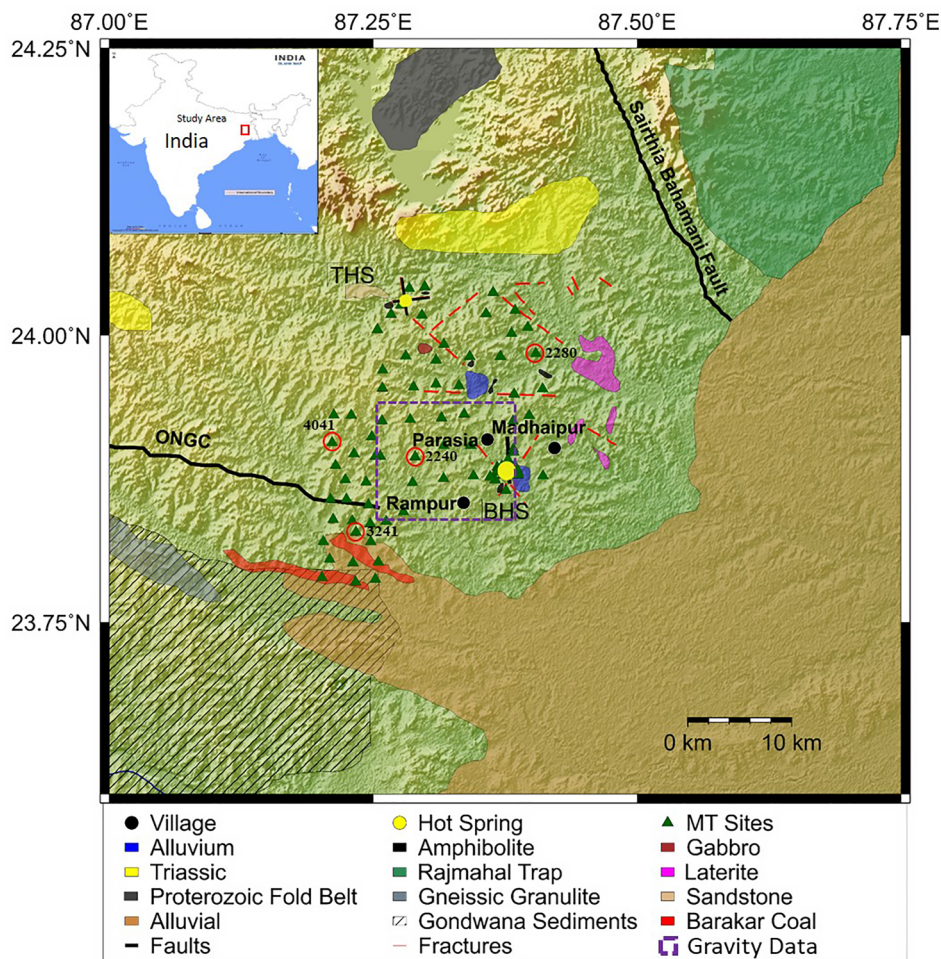


**FIGURE 1** Geological map of the Bakreswar geothermal province with the locations of magnetotelluric (MT) sites (green triangles). All geological domains are plotted over the background of the Chotanagpur Granite Gneissic Complex (CGGC). Black solid lines: deep-seated fault (Majumdar et al., 2000; ONGC, 1969); yellow circles: Bakreswar (BHS) and Tantloie (THS) hot springs. Red unfilled circles mark MT stations (labelled) for which observed data are shown in Figure 2, and the data for all the sites used in the study are shown in Appendix A and B. Purple dashed rectangle shows the region over which the gravity data (Sinharay, 2006) are available and have been used in this study.

## GEOLOGY

The Bakreswar geothermal province is located over the Archaean gneisses and schists formations of the Chotanagpur Granite Gneissic Complex in the eastern part of the Indian Peninsular Shield (Figure 1). The area has undergone different cycles of plate movements with periods of isostatic readjustments during the Precambrian to Cenozoic times (Dunn, 1939, 1941; Desikachar, 1974; Ghosh, 1948; Sarkar, 1982). The rocks in the region are highly sheared, brecciated and mylonitised near the springs (Nagar et al., 1996; Mukhopadhyay, 1996). The Chotanagpur plateau is host to several groups of hot springs which can be attributed to the deep circulation of meteoric water along the major fractures that have been newly created or reactivated in the crystalline basement due to tectonic disturbances in the terrain (Deb & Mukherjee, 1969). The hot spring occurs along the fractures associated

with faulted contacts of the Gondwana sediments in the coal belt of Birbhum which is aligned north–south and the Rani-ganj Jharia coalfield aligned east–west (Sinharay et al., 2010). The Bakreswar hot spring (BHS) is surrounded by alluvial and laterite soil with the sporadic exposure of basement rocks consisting of granitic gneiss with minor enclaves of calc-silicate, amphibolite, gabbro, pegmatite and dolerite (dykes) (Majumdar, 2000; Majumdar, 2009). These gneisses and calc-silicates are folded regionally to northeast–southwest-oriented asymmetric to symmetric anticlinal and synclinal structures (Nagar et al., 1996). Based on Wenner resistivity profiling and vertical electrical sounding results, four sets of vertical to sub-vertical joints with oblique directions intersect the basement rock close to the BHS (Majumdar et al., 2000). An NS striking buried fault with a maximum depth of ~40 m in the vicinity of the BHS has been mapped. This fault has a downthrown block in the east and is marked by an approximately 1.5

km long brecciated and silicified zone north of the BHS (Majumdar et al., 2000). The fractures in the crystalline basement and faults are supposed to define the required environment for the circulation of hot fluids (Majumdar et al., 2000; Sinharay et al., 2010). The Tantloie hot spring is situated at the northern margin of the study area. This hot spring which lies along two smaller faults is related with the boundary fault between the Precambrian and Gondwana rocks (Mukhopadhyay, 1989; Nagar et al., 1996). A deep-seated fault (Oil and Natural Gas Corporation [ONGC]) striking roughly east–west was mapped by ONGC, India (Majumdar et al., 2000; ONGC, 1969) and is present in the western part of the study area (solid black line in Figure 1). It also runs parallel to the main axis of the sedimentary deposits of the Gondwana formations (Majumdar et al., 2000) comprising important coal fields such as the Bokaro, Jharia, Karanpura, Ramgarh and Raniganj (Ghosh et al., 1993) (area with slanted black lines in Figure 1).

## MAGNETOTELLURIC METHOD

Magnetotelluric (MT) method is a natural-source electromagnetic (EM) method which maps the electrical conductivity structure of the Earth. It involves simultaneous measurements of total EM fields, that is, time-varying magnetic fields and induced electric fields (Cagniard, 1953; Tikhonov, 1950). Subsurface conductivity structure is determined from the relationship between two horizontal components of the measured electric fields ( $E_x$  and  $E_y$ ) and three components of magnetic fields ( $H_x$ ,  $H_y$  and  $H_z$ ).

The relationships between amplitude and phase of the horizontal components of the EM field given by Equation (1) are represented by a frequency dependent second rank tensor, known as impedance tensor  $Z$  (Simpson & Bahr, 2005)

$$\begin{pmatrix} E_x \\ E_y \end{pmatrix} = \begin{pmatrix} Z_{xx} & Z_{xy} \\ Z_{yx} & Z_{yy} \end{pmatrix} \begin{pmatrix} H_x \\ H_y \end{pmatrix}. \quad (1)$$

The amplitude of  $Z$  is termed apparent resistivity and calculated by

$$\left( \rho_{a_{ij}} = 0.2T \left| Z_{ij} \right|^2 \right), \quad (2)$$

where  $i, j = x, y$  and  $T$  is the time period, whereas the imaginary part is termed phase and calculated by

$$\left( \phi_{ij} = \arg \left( Z_{ij} \right) \right). \quad (3)$$

Induction arrows are the vector representation of the complex ratios of vertical to horizontal magnetic field components (Vozoff, 1972) and represented as Equation (4). These arrows

are used to infer the lateral variation in conductivity. These vectors are also referred to as tipper vectors ( $\mathbf{T}$ ):

$$H_z(\omega) = \left( T_x(\omega) \ T_y(\omega) \right) \begin{pmatrix} B_x/\mu_0 \\ B_y/\mu_0 \end{pmatrix}. \quad (4)$$

Caldwell et al. (2004) and Bibby et al. (2005) introduced the concept of phase tensor (PT) for the analysis of MT data, especially the galvanically distorted data. PT is graphically represented as an ellipse whose major and minor axes represent the principal axes of the tensor which reflect lateral variations in the underlying regional conductivity structure (Caldwell et al., 2004).

A phase is also related with each component of  $\mathbf{Z}$ . The relation can be expressed as second rank 2D tensor, referred to as PT  $\varphi$ .

$$\varphi = X^{-1}Y = \begin{pmatrix} \varphi_{11} & \varphi_{12} \\ \varphi_{21} & \varphi_{22} \end{pmatrix}, \quad (5)$$

where  $\mathbf{X}$  and  $\mathbf{Y}$  denote the real and imaginary parts of  $\mathbf{Z}$ , respectively.

The near-surface conductivity heterogeneities cause distortions of the electric fields which causes distortions in impedances data, known as the galvanic effect. Due to this effect, the amplitude information present in the regional impedance tensor cannot be recovered from the measured impedance data.

The most important characteristic of this method is that it makes no assumptions about the dimensionality of the regional response tensor and is unaffected by the presence of electric field galvanic distortion. The geometry of PT ellipse is an indicator of the directionality and dimensionality of the MT data.

## DATA SET

### Magnetotelluric data acquisition and processing

Magnetotelluric (MT) data in the frequency range of 10 kHz–10 Hz were acquired using the MTU-5A system of Phoenix Geophysics Ltd. Pb/PbCl<sub>2</sub> electrodes and AMTC-30 induction coils have been used to measure the horizontal components of the electric field and all the components of the magnetic field, respectively. The lengths of the electrical dipoles were about 100 m. MT data were acquired in two different experiments: (a) 71 sites having an average site spacing of 1.5–3 km and (b) 24 sites having an average site spacing of ~250 m in the close vicinity of Bakreswar hot spring (Figure 1). The MT data were processed using the EMERALD software package (Ritter et al., 1998, 2015; Weckmann et al.,

2005). To further reduce the scattered data points, a statistical approach using the Mahalanobis distance (MD) criteria (Platz & Weckmann, 2019) was applied. In this approach, MD is used to classify the distribution of MT transfer functions through their distance. The MD is an important distance measure for multivariate data. It represents a generalization of the well-known Euclidean distance and allows for correlated data by taking the inverse of the covariance matrix into account. As electromagnetic noise often forms a completely independent cluster of transfer functions, the MD criterion is able to remove such clusters as well as to reduce scatters around the desired cluster of MT transfer functions.

## Gravity data

Gravity data (Figure 1; purple dashed rectangle) in the region from Sinharay (2006) have been used in this study.

## MAGNETOTELLURIC DATA ANALYSIS

The observed magnetotelluric (MT) data responses for four representative sites (2240, 2280, 3241 and 4041) located in different parts of the study area (Figure 1) are shown in Figure 2. All four impedance tensor components are displayed in terms of apparent resistivities (upper panel) and phases (middle panel), together with the vertical transfer function data (lower panel). The quality of the data is good as the scatters and standard deviations are in general low. In general, resistivities vary from 100 to 1000  $\Omega\text{m}$  except for a few sites for which resistivities in the decade between 100 and 10 Hz are higher than 1000  $\Omega\text{m}$ . The average resistivity value for the highest frequencies (10,000–1000 Hz; and thus, shallowest penetration depth) for the majority of the sites is  $\sim 200 \Omega\text{m}$ . Although the data were acquired for 95 MT sites, we have used (a) 65 sites for a regional study and (b) 24 sites located close to the Bakreswar hot spring (BHS) for a localized study around BHS. These 24 sites have an average site spacing of  $\sim 250$  m which satisfies the horizontal resolution limits required to map the 1.5 km long NS striking fault under the alluvial cover with a maximum depth of  $\sim 40$  m in the vicinity of the BHS as reported by Majumdar et al. (2000). The observed data used for the regional study have been plotted in Figure A.1a–c, whereas those used for the localized study around the BHS have been shown in Figure B.1.

## STRIKE AND DIMENSIONALITY ANALYSIS

The dimensionality analysis has been performed using the concept of phase tensor (PT) (Caldwell et al., 2004). The prin-

cipal axes and their orientation of PT ellipses represent the direction of the maximum and minimum phase values and hence the direction of the maximum and minimum induction currents (Caldwell et al., 2004). Directionality and dimensionality of the data set can be inferred through analysing the geometry of the PT ellipses and their pattern in map view, such as the parameters of the maximum  $\Phi_{\text{max}}$  and minimum  $\Phi_{\text{min}}$  phase values, the skew angle  $\beta$  and the angle  $\alpha$ .

For more details, we refer the readers to an extensive literature (e.g. Bibby et al., 2005; Caldwell et al., 2004; Marti, 2014; Weaver et al., 2000). PT ellipses along with induction vectors in Wiese convention (Wiese, 1962) (real arrows point away from the conductors) for all sites are plotted for the observed frequencies of 1024 Hz (Figure 3a), 512 Hz (Figure 3b) and 16 Hz (Figure 3c), whereas the same plot for remaining frequencies has been shown in Figure S1. To analyse the dimensionality, we used the criterion  $|\beta| > 3^\circ$  for data requiring a three-dimensional (3D) interpretation. For all three frequencies, 1024, 512 and 16 Hz, the majority of data seem to require a 3D interpretation as most of the skew angles  $|\beta|$  are more than  $3^\circ$  and also the induction vectors are oriented in random directions.

The induction vectors (Figure 3) allow to identify first-order electrical conductivity anomalies. We find a reversal on both sites of line C1 for 512 Hz indicating an enhanced electrical conductivity along C1. Another change of direction occurs on both sides of line C2; although we do not observe a full and clear reversal, the induction vectors point roughly into opposite directions. In addition, sites close to the Bakreswar hot spring have small or negligible induction vectors indicating the absence of large electrical conductivity anomalies. Towards the south of the study area, we observe north-pointing induction vectors which seem to be caused by a more conductive structure existing further south of the study area.

Majority of sites are affected by (local) 3D structures and do not fulfil the 2D criteria. The variation observed in the orientation of the phase-tensor ellipses and the induction vectors shows a complex subsurface structure in the region. Therefore, 3D inversion of the entire data set is required and in general possible due to the areal experimental layout.

## THREE-DIMENSIONAL INVERSION AND RESULTS

Three-dimensional (3D) inversion of magnetotelluric (MT) data has been performed using ModEM, the modular electromagnetic (EM) modelling and inversion algorithm (Egbert & Kelbert, 2012; Kelbert et al., 2014; Meqbel, 2009). This code uses the non-linear conjugate gradient algorithm which aims towards the minimization of the penalty function. The distribution of sites in the study area is uneven, with a rather

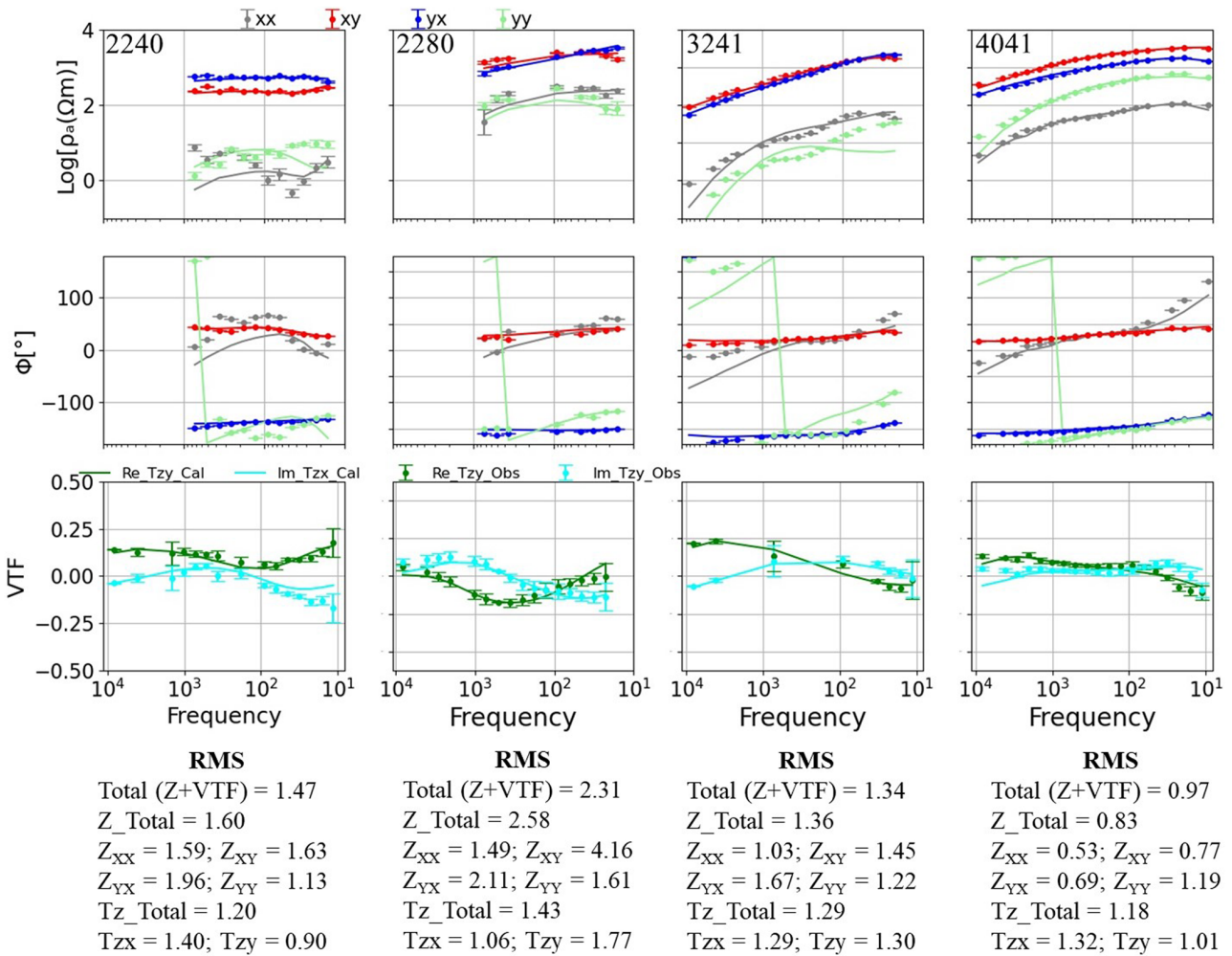


**FIGURE 2** Observed (symbols) and predicted (lines) apparent resistivity (top row), phase (middle row) and vertical transfer function data (real and imaginary parts) (bottom row) for some representative sites (2240, 2280, 3241 and 4041). Some frequencies had to be masked if the data quality could not be improved satisfactorily.

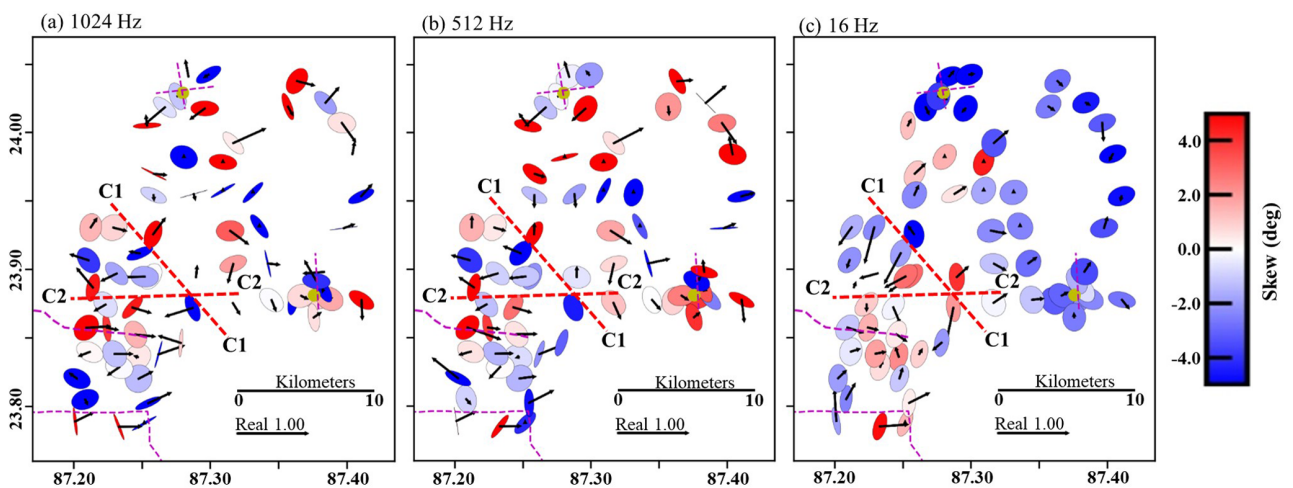


**FIGURE 3** Map view of phase tensors coloured by skew angle  $\beta$  and real induction vectors in Wiese convention (Wiese, 1962) for frequencies of 1024 (a), 512 (b) and 16 Hz (c). Dashed red lines C1 and C2 mark zones, which show a reversal of the induction vectors. Yellow circles mark the location of Bakreswar (BHS) and Tantloie (THS) hot springs. The dashed magenta lines indicate the position of faults close to the hot springs, Oil and Natural Gas Corporation (ONGC) fault and the northern boundary of Gondwana sediments as shown in Figure 1.

dense site spacing in the vicinity of the Bakreswar hot spring (BHS), whereas in other parts, the site distances are 10 times larger. Therefore, we tested different grids to find an optimal compromise between model resolution, numerical stability and computational costs/resources. We observed severe challenges in the vicinity of the BHS where a much denser and uneven site spacing resulted in an increased focus and weight of the inversion in those regions. Ultimately, the inversion resulted in circular high-resistivity zones. However, the measured data do not justify these high resistivities. Therefore, we divided our inversion procedure into two parts: (a) a regional study by inverting 65 sites (selection of sites was based on noise conditions and those with an even site separation to ensure an even grid size for inversion), and (b) a localized study in the vicinity of BHS by inverting 24 sites located in the direct vicinity of the BHS with an even and very small site spacing ( $\sim 250$  m). Out of the total 95 sites, 65 sites were used for regional inversion, and 24 sites were used for localized studies. There are five sites which are common to both regional and localized studies. Eleven sites have been removed due to poor data quality.

## Regional study

A two-step inversion approach was used for the regional study involving 65 sites. However, we initially omitted five stations (0010, 0130, 0040, 0070 and 1100) near the hot springs and later-on included those again. The initial model comprised a grid of  $263 \times 263 \times 100$  km<sup>3</sup>, discretized into  $122 \times 112 \times 68$  cells with a side length of 400 m along the  $x$  and  $y$  directions in the inner part. The shallow surface heterogeneities distort apparent resistivity data by a scaling factor while keeping the phases unchanged, which causes severe static shift to the model results. To compensate for the static shift and galvanic distortions caused by shallow inhomogeneous bodies, a fine mesh model discretization is needed in the vertical direction at shallow depths (Meqbel et al., 2014; Xiao et al., 2010). Along the vertical axes, the first upper 200 m are divided into cells with equal thickness of 10 m, whereas from a depth of 200 m down to 1 km, the thickness increased by a factor of 1.1. Eventually, the cell thickness increased by a factor of 1.2 from a depth of 1 km down to 10 km. Subsequently, the thickness of the cells increased with depth by a factor of 1.3. Several inversions were performed with different settings for the error floors of all four impedance components and components of the vertical transfer function (VTF) data. We used several values of error floor ranging from 5% to 20% for the main diagonal components and 2% to 10% for the off-diagonal components. On the basis of low RMS and better misfit between the observed and the predicted data, we selected the final error floor settings for each components as  $Z_{xx} = 10\%$  of  $\sqrt{|Z_{xx} \cdot Z_{yy}|}$ ;  $Z_{yy} = 10\%$  of  $\sqrt{|Z_{yy} \cdot Z_{xx}|}$ ;  $Z_{xy} = 5\%$  of  $|Z_{xy}|$ ,  $Z_{yx} = 5\%$  of

$|Z_{yx}|$  and  $Z_{yy} = 10\%$  of  $\sqrt{|Z_{yx} \cdot Z_{yy}|}$ . The final error floor setting for the vertical transfer data was chosen as 0.02.

In addition to the above error floor settings, the error floor for the off-diagonal components was reduced to 2% for the frequency range between 100 and 10 Hz to better fit the data at lower frequencies.

3D inversion of MT data as a non-linear inversion problem requires an iterative minimization process of the data fit and the regularization against a starting or prior model together with a smoothness constraint. Therefore, the choice of the initial model can influence the result (Hersir et al., 2013). The starting models utilized in 3D inversions were homogenous half spaces of 100, 200, 500, 1000, and 1500  $\Omega$ m, not including a priori information. 3D inversions using a combination of impedance tensor  $Z$  and VTF data were performed for regional modelling (without the five sites close to the BHS). Figure C.1 shows a comparison of convergence of RMS for inversions performed using different half-spaces possessing different resistivity values, namely 100 (green line), 200 (black line), 500 (red line), 1000 (blue line) and 1500  $\Omega$ m (yellow line), respectively. The RMS converges from 10.47, 10.45, 13.44, 19.40 and 24.68 to 2.5, 2.23, 2.47, 2.70 and 2.68 for half space model of 100, 200, 500, 1000 and 1500  $\Omega$ m, respectively. Although the starting RMS of the resistive half space was highest, within 40 iterations all models despite their different starting resistivities arrived at a similar RMS value.

Figure 4 shows a comparison of 3D resistivity models obtained from the inversion of different initial uniform half space resistivities of 100 (Figure 4a), 200 (Figure 4b), 500 (Figure 4c), 1000 (Figure 4d) and 1500  $\Omega$ m (Figure 4e) in form of horizontal slices at depth of  $\sim 2.5$  km. We observe most structural details for the 200  $\Omega$ m resistivity model. The inversion model using the 200  $\Omega$ m initial half space represents a good compromise between structural details and coherent structures unlike the ones with 100, 500, 1000 and 1500  $\Omega$ m. Moreover, the model converges to minimum RMS value when 200  $\Omega$ m was used as initial resistivity model. The average resistivity for the highest frequency decade is 200  $\Omega$ m. Therefore, based on more structural diversity, minimum RMS and average value of highest frequency decade, a uniform half space resistivity of 200  $\Omega$ m was regarded as an initial model for performing inversion.

As stated earlier, we used a two-step approach to invert our data set. In the first step, we used both impedance and VTF data at 60 out of 65 sites, excluding the five sites close to the BHS. The final models obtained from the first step were used as the initial model for the first inversion to be performed in the second step. In the second step, five successive inversions were performed including one site after the other close to the BHS (0010, 0130, 0040, 0070 and 110). The final model from the previous inversion was always used as the initial model for the next inversion with the additional station included.

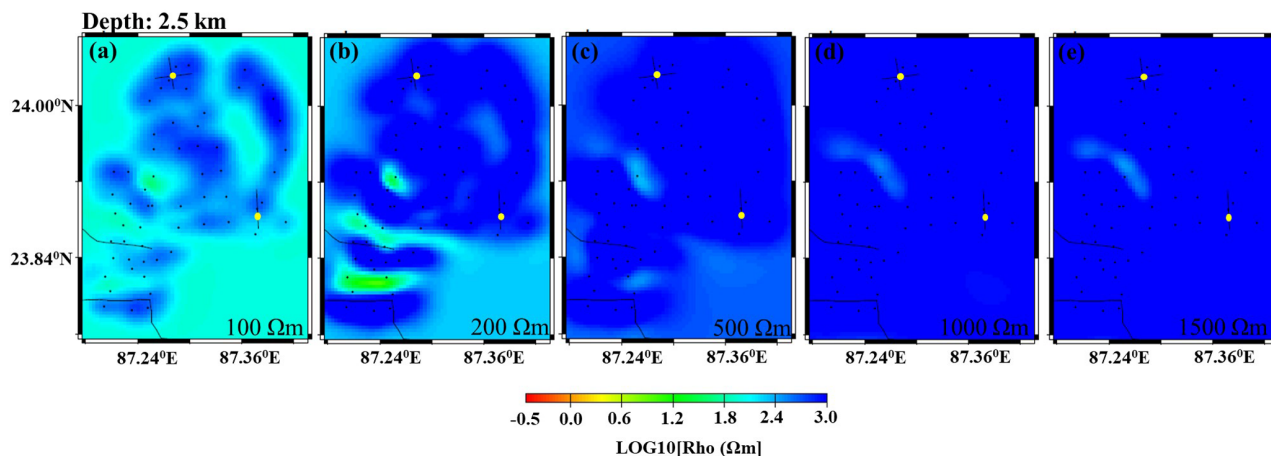


**FIGURE 4** Slices at 2.5 km depth of the 3D models obtained from different initial models: (a) 100, (b) 200, (c) 500, (d) 1000 and (e) 1500  $\Omega\text{m}$ . The yellow circles mark the location of Bakreswar (BHS) and Tantloie (THS) hot springs. Solid black lines indicate the position of faults close to the hot springs, Oil and Natural Gas Corporation (ONGC) fault and the northern boundary of Gondwana sediments as shown in Figure 1.

To obtain an impression on the resulting data fit, we show the predicted curves corresponding to the final inversion model using 65 sites for the representative sites (2240, 2280, 3241 and 4041) in Figure 2, whereas observed and predicted data (resistivity and phase) for all the sites are shown in Appendix A. Apparent resistivity and phase data for the off-diagonal components of the observed and predicted data show a good match for almost all the stations, whereas for the main diagonal components, majority of the sites show a good match except for some sites in the upper central part which may be due to severe noise conditions and scatters in the data set. The VTF data also show a good match for all the stations. The strategy of inverting the data set in 2 stages helped in lowering the final RMS to 2.21 instead of 2.59 when all 65 sites were inverted at once.

As the final 3D model (Figure 6) involves a combination of both impedance  $Z$  and VTF data, we need to display the RMS associated with each of these components separately to better assess problems in data fitting. The RMS distribution maps have been plotted for the combination of impedance  $Z$  and VTF data (Figure 5a),  $Z$  (Figure 5b) and VTF (Figure 5c). The RMS distribution map for the combination of impedance  $Z$  and VTF data (Figure 5a) exhibits that the RMS is evenly distributed in most parts of the study area. However, it also shows a couple of sites with higher RMS values in the upper central part. High RMS values for these sites are linked to severe noise conditions and scattering present in the data set.

To show consistency between the final model and the observed data, a comparison of the phase tensor ellipses coloured with values of skew angle  $\beta$  for observed data and predicted data of the preferred 3D model at 90.5 Hz are plotted for all the sites in Figure D.1. There is a good match between observed and predicted ellipses which shows that the final model (Figure 6) is consistent to the observed data.

Horizontal slices of the preferred 3D model have been plotted at various depths, namely  $\sim 500$  m (Figure 6a),  $\sim 1.25$  km (Figure 6b),  $\sim 1.7$  km (Figure 6c), and  $\sim 2.5$  km (Figure 6d). The vertical cross sections along C1, C2 and C3 are shown in Figure 6e–g. If we look at the final 3D model in terms of horizontal slices at depths of 500 m, 1.25 km, 1.7 km and 2.5 km (Figure 6), we can identify several consistent electrical conductivity anomalies. A linearly shaped conductive feature C1 with less than 50  $\Omega\text{m}$  starts at a depth of 250 m down to 2.5 km, which is at the same position as the reversal of the observed induction vectors (see Figure 3). Due to the sparse station coverage, we observe several patches with resistivity values less than 10  $\Omega\text{m}$  within the conductive zone C1, and these features are not connected. The conductive anomaly (C1) is sandwiched between resistive features at the northern and southern side. To check if the conductive patches observed in feature C1 are connected, a denser MT site spacing around C1 is required. The conductive feature C2 (Figure 6d) with less than  $\sim 50$   $\Omega\text{m}$  lies approximately 1 km north of the mapped Oil and Natural Gas Corporation (ONGC) fault and is observed in a depth range between 2 and 3.7 km. In the 3D model, the conductive anomalous features C1 and C2 merge at a depth of 2.3 km continuing further downwards (Figure 6d). Interestingly, there is no conductive zone directly related (at least not spatially) with the ONGC fault (marked in Figure 1; Majumdar et al., 2000) but it lies at the boundary of C2 at a depth of 2.5 km. Due to the given experimental layout with no MT sites south of the BHS, the eastward extension of C1 cannot be mapped. Another conductive anomaly C3 which is also evident from the induction vector plot (see Figure 3) is located parallel to the conductive feature C2.

To check whether the MT data require the existence of the conductivity anomalies C1, C2 and C3 and if they

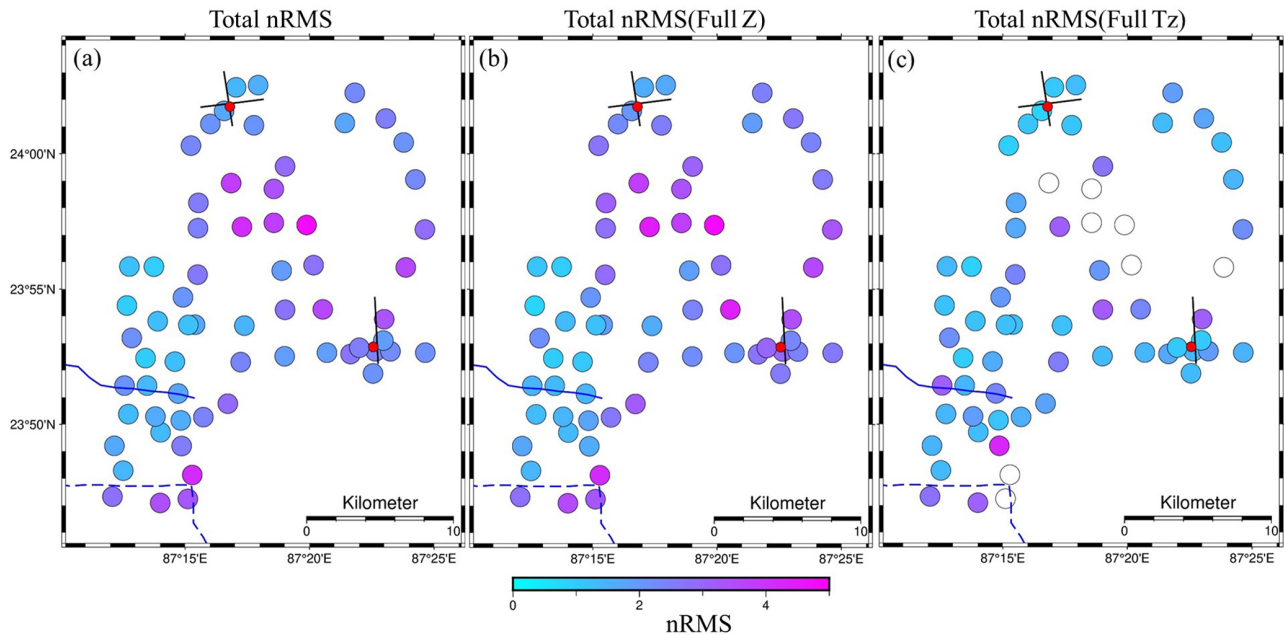


**FIGURE 5** Map of the total RMS corresponding to (a) Z + VTF, (b) Z and (c) vertical transfer function (VTF) data of the final regional 3D inversion model. White filled circles in (c) denote the absence of VTF data for these sites. Red circles indicate Bakreswar (BHS) and Tantloie (THS) hot springs. Solid black lines indicate faults close to the hot springs, solid blue line indicates the Oil and Natural Gas Corporation (ONGC) fault, and the blue dashed line marks the northern boundary of Gondwana sediments.

support their position and shape, we replaced these features by cells with higher resistivities of 500  $\Omega\text{m}$ . We used the modified models (Figure 7a,b) to perform forward calculations and compare the predicted data with the observed data (Figure 8). If the data require the conductivity anomalies, we expect that the predicted data obtained from the modified models show much larger RMS values than the data calculated in 3D inversion.

To evaluate the data fits, we have computed ratios between the RMS of the predicted data obtained from the forward calculation of the perturbed model ( $\text{RMS}_p$ ) and the RMS for the predicted data obtained after the original 3D inversion ( $\text{RMS}_0$ ) (Figure 8). We introduced three different classes: If the RMS is identical within a 10% range, we retrieve ratios between 0.9 and 1.1; otherwise, the data fits are worse. The overall RMS for the perturbed model increases from 2.21 to 3.39, which is not surprising since in the region where the anomalies have been modified white circles indicate a worsened data fit. The green circles in the north-eastern part of the model mainly exhibit values around 0.9–1.1 suggesting that the data fit has not changed. In summary, anomalies C1, C2 and C3 seem to be required by the measured MT data.

To determine the maximum depth of exploration, we performed a forward modelling study by including a conductive layer of 1  $\Omega\text{m}$  at various depths: (a) 2.0–3.0; (b) 3.23–4.45; (c) 4.55–5.25; (d) 5.25–6.21; (e) 6.21–7.36 km; and RMS between the data obtained after forward modelling and the observed data is 4.04, 2.68, 2.31, 2.24 and 2.20, respectively.

We determined the depth of exploration by comparing the new RMS values with the one of our final models, as we expect a worsened data fit once the conductive layer deteriorates the model response in the available period range (Singh et al., 2019). As a result, we can conclude that the model is sensitive to the conductive layer down to a depth of 5.25–6.21 km where the RMS worsens in comparison to the RMS obtained for the preferred 3D inversion model.

### Localized study in the vicinity of Bakreswar hot spring

The closely spaced MT sites in the vicinity of the BHS could not be included in the main inversion because of the two reasons: (a) The cell size of regional model was larger than the site spacing in the vicinity of the BHS and (b) having a regional model with the cell dimensions required by the dense site spacing, the resulting model is too large, invites artefacts and is computationally expensive. Adding, on the other hand, many stations in a confined area that need to be fitted overemphasizes the impact of this region in contrast to the remaining part of the model. Therefore, a separate inversion was performed using 24 MT sites located around the BHS.

To obtain an optimized value of initial resistivity of the homogeneous half-space, inversions were performed using all the impedance components and the VTF data using resistivities of 100, 200, 500 and 1000  $\Omega\text{m}$  which converged to

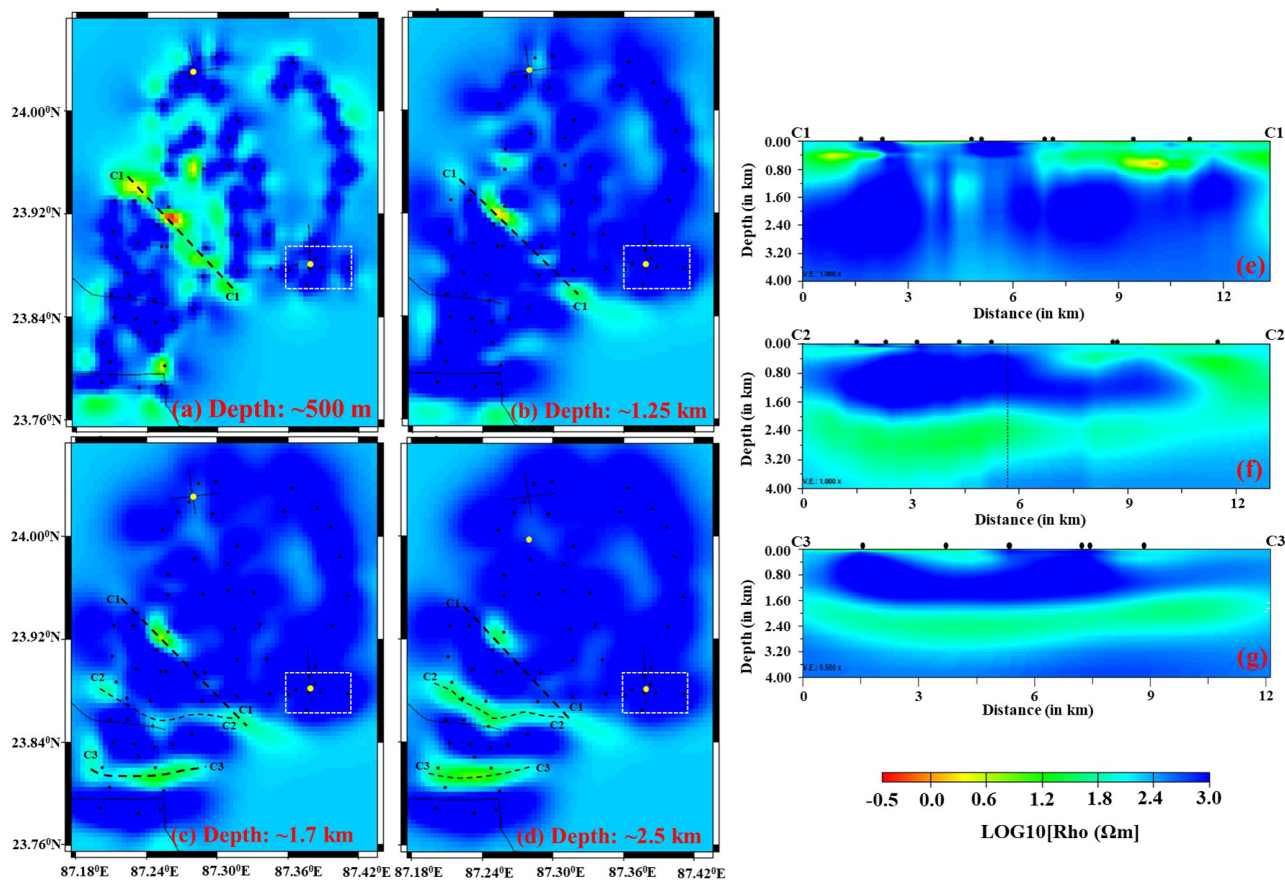


**FIGURE 6** Horizontal slices of the preferred 3D model at various depths. (a)  $\sim 500$  m, (b)  $\sim 1.25$  km, (c)  $\sim 1.7$  km, (d)  $\sim 2.5$  km, (e) vertical cross section along C1, (f) vertical cross section along C2 and (g) vertical cross section along C3. The yellow circles (a)–(d) mark the location of Bakreswar (BHS) and Tantloie (THS) hot springs. The solid black lines indicate the position of faults close to the hot springs, Oil and Natural Gas Corporation (ONGC) fault and the northern boundary of Gondwana sediments as shown in Figure 1. The white dashed rectangle shows the region over which the localized study around BHS has been performed.

RMS values of 2.38, 2.26, 2.16 and 2.21, respectively. The 3D models corresponding to the above-mentioned homogeneous half-space resistivity values maps similar conductive features. Therefore, on the basis of low RMS criteria, better misfit of sounding curves between observed and predicted data, and the fact that the average values of resistivities for the highest frequency was 500, 500  $\Omega\text{m}$  was selected as an optimal starting model. The size of initial model was  $60 \times 61 \times 100 \text{ km}^3$  discretized into  $62 \times 72 \times 68$  cells, with the dimension of 100 m along  $x$  and  $y$  directions. Along the vertical axes, the first upper 200 m are divided into cells with an equal thickness of 10 m, whereas from a depth of 200 m to 1 km, the thickness increased by a factor of 1.1, following a factor of 1.2 from a depth of 1 km down to 10 km. Subsequently, the thickness of the cells increased with depth by a factor of 1.3. Several inversions were performed with different settings for the error floors of all four impedance components and components of the VTF data. The final 3D inversion was performed for all the components of impedance and VTF data incorporated an error floor values of error floor for each of the component

as  $Z_{xx} = 10\%$  of  $\sqrt{|Z_{xy} \cdot Z_{yx}|}$ ,  $Z_{xy} = 5\%$  of  $\sqrt{|Z_{xy} \cdot Z_{yx}|}$ ,  $Z_{yx} = 5\%$  of  $\sqrt{|Z_{xy} \cdot Z_{yx}|}$  and  $Z_{yy} = 10\%$  of  $\sqrt{|Z_{xy} \cdot Z_{yx}|}$  and 0.02 for all the components of vertical transfer data. The final model converged to RMS of 2.16 in 99 iterations. To analyse the performance of the inversion process, we show observed and predicted data (resistivity and phase) for all the 24 sites in Figure B.1. Apparent resistivity and phase data for the off-diagonal components of the observed and predicted data show a good match for almost all the stations, whereas a reasonable match is observed for the main diagonal components.

The final 3D model in terms of horizontal slices shows electrical structures at depths  $\sim 0.05$  km (Figure 9a) and  $\sim 0.10$  km (Figure 9b). Conductive structures L1, L2 and L3 of 10  $\Omega\text{m}$  are located close to the BHS. These conducting structures are not connected to each other (Figure 9a). The vertical cross-section (Figure 9c) shows the presence of a shallow conductive feature up to a depth of  $\sim 50$  m all along the profile. The features L1, L2 and L3 are observed at a maximum depth of  $\sim 50$  m which is less than the minimum skin depth ( $\sim 120$  m) for a homogeneous half resistivity of 500  $\Omega\text{m}$  and 10,000 Hz.

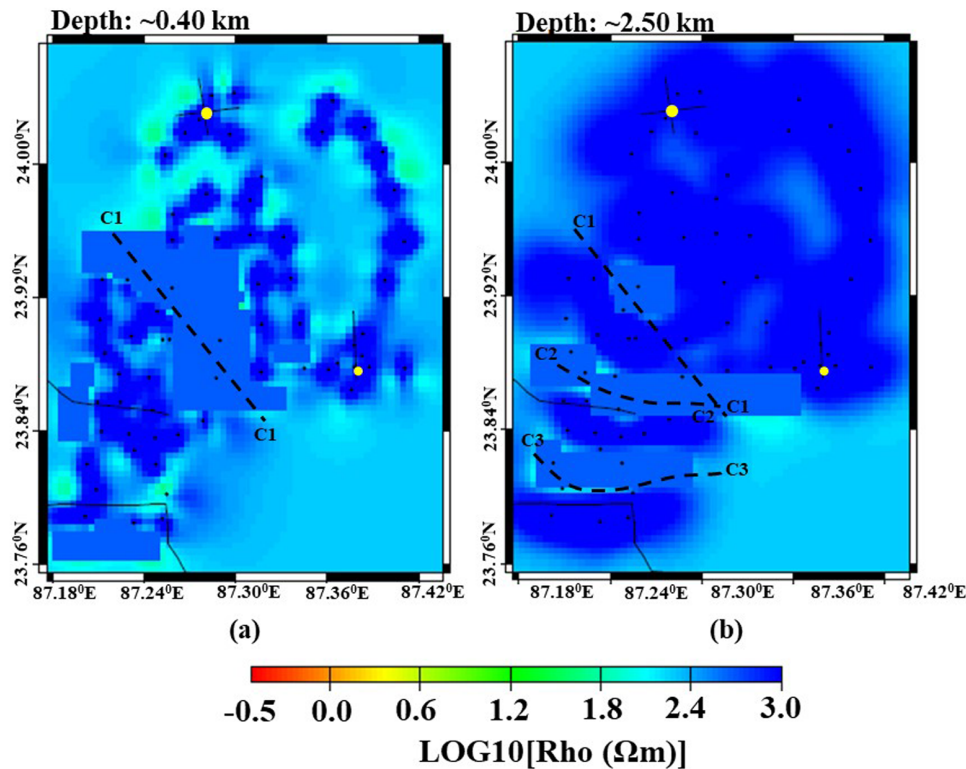


**FIGURE 7** Modified 3D model after replacing the resistivity values of the anomalies C1, C2 and C3 by a block with constant resistivity of 500  $\Omega\text{m}$  at depths (a)  $\sim 0.40$  km and (b)  $\sim 2.50$  km. The yellow circles mark the location of Bakreswar (BHS) and Tantloie (THS) hot springs. Solid black lines indicate the position of faults close to the hot springs, Oil and Natural Gas Corporation (ONGC) fault and the northern boundary of Gondwana sediments as shown in Figure 1.

Therefore, these features can only be detected but cannot be resolved. However, resistivity studies done over the area (Majumdar et al., 2000) have concluded that the occurrence and movement of fluid take place mostly in the weathered and fractured crystalline basement rocks at shallow depths.

## INTERPRETATION

The three-dimensional (3D) inversion models of the magnetotelluric (MT) data imaged conductive and resistive features present in the area which are discussed in detail as follows:

### Northwest–southeast striking conductive feature (C1)

The phase tensor analysis (Figure 3) suggests the presence of a prominent northwest–southeast (NW–SE) striking electrical conductive structure that seems to correlate with the conductivity anomaly C1 (Figure 6). The resistivity of this anomaly is  $\sim 100 \Omega\text{m}$ , and it contains areas with significantly lower resistivities. The conductive zone C1 extends from a depth of 250 m to  $\sim 2.5$  km in the central part and shallows towards both

sides, and seems to divide the study area into two resistive regions. Due to its depth extent upto 2.5 km in the central part, it acts as path for the geothermal fluid to reach the deeper level of the geothermal setting where it gets heated and rises up to shallow depth. Due to the limited site coverage towards the south of the Bakreswar hot spring (BHS), a possible extension of C1 is speculative.

Available gravity data (Sinharay, 2006) in the region have been used to corroborate the presence of the NW–SE striking conductive anomaly C1. The Bouguer gravity anomaly map (Figure 10a) has been re-drawn after Sinharay (2006), where a significant Bouguer anomaly of +26 mGal is observed at the NW end of the area where gravity data were collected (see purple box in Figure 1). A high Bouguer anomaly ( $>20$  mGal) which stretches NW–SE is wider at the NW end and narrows towards the SE of the survey area. It separates the study area into two zones of relatively low Bouguer anomalies ( $<20$  mGal). This NW–SE-oriented feature (Figure 10a) coincides with the conductivity anomaly C1 trending in NW–SE direction (Figure 6). The NW–SE orientation of Bouguer anomaly is identical to the orientation of the resistivity anomaly as observed in the resistivity section of the 3D model (Figure 6) at a depth of  $\sim 500$  m (Figure 10b).

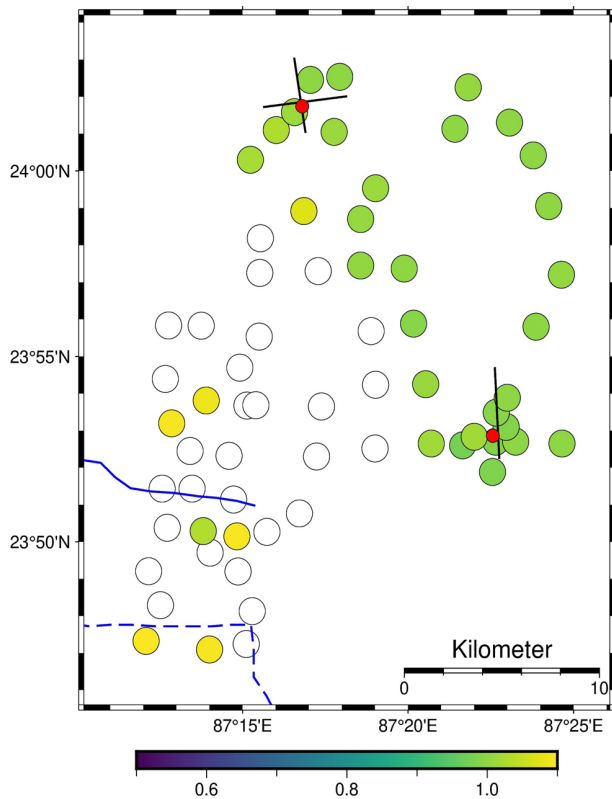


**FIGURE 8** Map of the ratio of  $RMS_p/RMS_0$  for all magnetotelluric (MT) sites used in the inversion. The red circles mark the location of Bakreswar (BHS) and Tantloie (THS) hot springs. Solid black lines indicate faults close to the hot springs, solid blue line indicates the Oil and Natural Gas Corporation (ONGC) fault, and the blue dashed line marks the northern boundary of Gondwana sediments.

The high gravity zones can be linked to the intrusion of high-density basic/ultrabasic igneous rocks from the deeper parts of the Earth (Kumar & Ahmad, 2007) suggesting that the high values of the NW–SE trending gravity anomaly ( $>20$  mGal) may be associated with the intrusion of these type of rocks. In the NW part of the Bouguer gravity contour map (Figure 10a), sharp horizontal gradient is observed which may be indicative of a fault (?). This is attributed to the fact that faulting causes re-distribution of density across the fault plane resulting in the juxtaposition of rocks of different densities. NW–SE gravity contours greater than  $+20$  mGal suggest that the central region may be the upthrow side of the fault, whereas comparatively low gravity values less than  $+20$  mGal towards the NE and SW suggest that this is the downthrow side of the fault.

Tilt angle derivatives (TDR; Fairhead et al., 2008; Salem et al., 2007, 2008; Saada, 2016) have been used to delineate the boundaries of the NW–SE trending feature (Figure 10a). Salem et al. (2007) described that the amplitude of the TDR varies from  $-\pi/2$  to  $\pi/2$  (radians) irrespective of the amplitude of the vertical derivatives. Values of the tilt angle close to zero over a plot of the spatial distribution of the TDR indi-

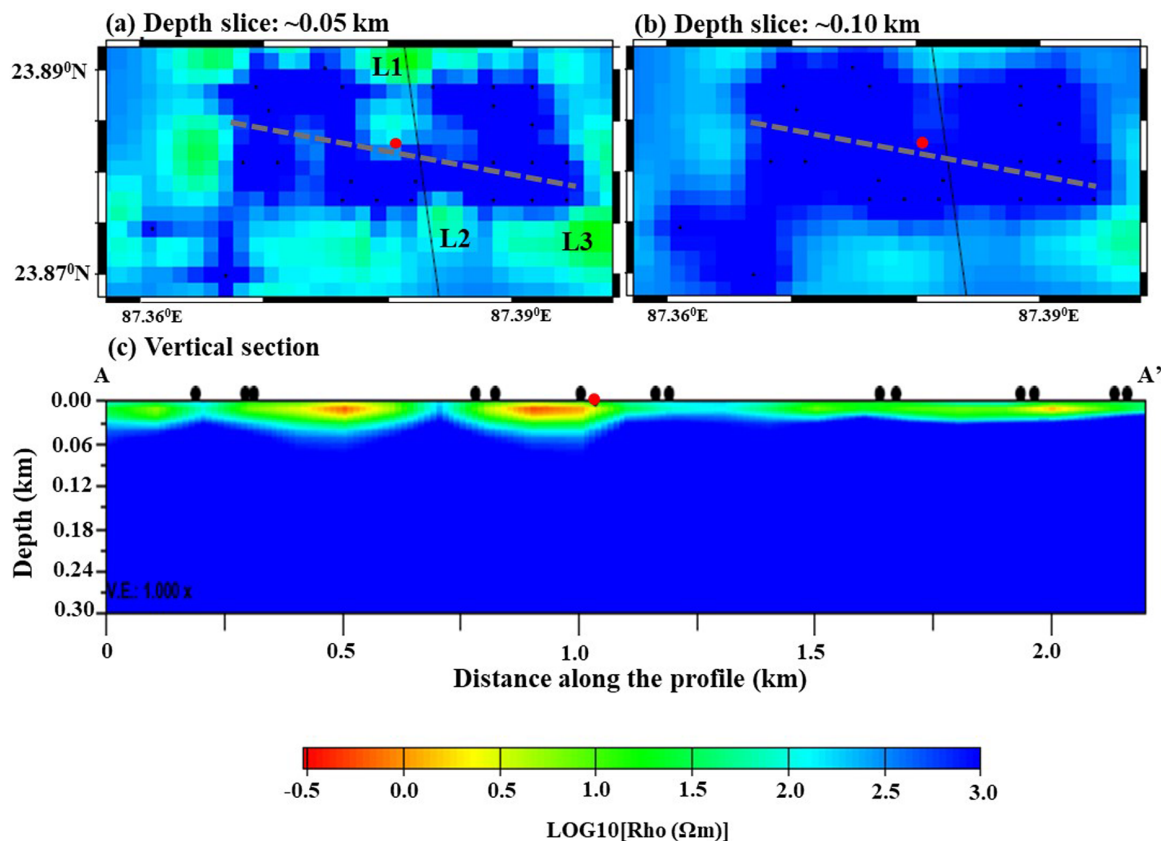
cate the top or the proximity to the source edge (Miller & Singh, 1994). Positive values are located directly above the source, whereas the negative values are located away from them. Figure 11 shows the TDR analysis of the Bouguer gravity data (Figure 10a). The zero-degree contour line (black line in Figure 11) indicates an abrupt change in density (sharp gradient) between positive and negative anomalies. Therefore, the zero-degree contour line seems to represent the boundary of the source. Positive values for the tilt angle (cyan line in Figure 11) can be found directly above the source. Negative values (magenta lines in Figure 11) are located farther away from the source.

Figure 11 shows the presence of an NW–SE trending structure which is indicated by positive values of the tilt angle. Possible candidates for these gravity anomalies could be the intrusion of high-density basic/ultrabasic igneous rocks. The central NW–SE trending positive values of the tilt angle might indicate the uplifted faulted block, whereas the negative tilt angles at the NE and SW end indicate the down faulted block. The NW–SE orientation of positive values of the tilt angles suggests an uplifted gravity source which is consistent with the orientation of the conductivity anomaly C1 (Figure 6) and with the orientation of high gravity values (Figure 10).

For a qualitative comparison, the TDR contour map (Figure 11) has been superimposed on conductivity depth slice of  $\sim 500$  m (Figure 12a) and  $\sim 2.5$  km (Figure 12b). The  $+0.785$  radian contour at a depth of 2.5 km (Figure 12b) confirms that this region represents the uplifted block of the fault and it acts as source to the high gravity Bouguer anomaly. This contour overlies the resistive features located to the north of C1 which hints the absence of water in this region. It suggests that the uplifted block acts as barrier to the movement of water.

It is remarkable to note that the  $0^\circ$  radian contour which also marks the boundary of the source (uplifted block) coincides with the embedded zones of significantly lower resistivities C1 (Figure 6) possibly indicating a fluid pathway.

To understand the structural relationship of NW–SE feature with the basement rocks, 2.5D gravity modelling was performed using Gravity and Magnetic Modelling Software. It is based on the method derived by Talwani et al. (1959) and Talwani and Heirtzler (1964) and uses the algorithm described by Won and Bevis (1987). This method calculates the gravity anomaly responses of different polygonal-shaped bodies having finite strike lengths. The model was extended on both sides of the profile up to several kilometres to avoid the edge effect. The regional Bouguer anomaly has been calculated using upward continuation of the Bouguer anomaly at a height of 10 km that approximates the anomaly response below 5 km (Jacobsen, 1987). The modelling has been carried out by considering three geological units: (a) sediments; (b) NW–SE trending high-density intrusive body and (c) granitic basement. The composition of high-density



**FIGURE 9** Horizontal slices of the preferred 3D model obtained from the inversion of the impedance and vertical transfer function (VTF) data for the sites located in the vicinity of the Bakreswar hot spring (BHS) at various depths: (a)  $\sim 0.05$  km depth; (b)  $\sim 0.10$  km and (c) Vertical cross section AA' (orange dashed line in a and b). The red circles mark the location of BHS. Solid black lines indicate faults close to the BHS. Orange dashed line in (a) and (b) is the profile over which vertical section shown in (c) has been extracted.

intrusive body is subalkaline, ranging in composition from basalt through basaltic andesite to andesite (Kumar & Ahmad, 2007). Following Telford et al. (1990), sediments, anomalous block and granitic basement have been assigned a density of 2.2, 2.8 and 2.64 g/cm<sup>3</sup>, respectively. The observed (black rectangle) and the predicted (solid line) residual gravity anomaly match well with an error of 0.09 (Figure 13). The gravity model (Figure 13) maps the presence of sediments at shallow depth all along the profile. The maximum depth of sediments is 300 m above the intrusive body (Figure 13). The high-density intrusive body extends from a depth of 600 m to 4.5 km. The high-density intrusive body is responsible for the NW–SE trending high Bouguer gravity contours (Figure 10a). These high dense intrusive body values of 2.8 g/cm<sup>3</sup> may be the upthrow side of the fault, whereas comparatively less dense material of 2.64 g/cm<sup>3</sup> is the downthrow side of the fault. Intrusion of the body indicates that the area is a relatively weak zone and there is the presence of fractures. These fractures can also promote the movement of water through this region (Majumdar et al., 2000).

## Conductive anomaly C2

Conductivity anomaly C2 (Figure 6) was mapped as an east–west trending feature with resistivities less than 50 Ωm extending from a depth of 2 to 3.7 km. When considering the location of the faults, they may act as conduits, barriers or combined conduit-barrier systems for the flow of geothermal fluids. The deep conductive anomaly C2 spatially correlates with the surface expression of a deep-seated fault (Gupta et al., 1976; ONGC, 1969; Shanker, 1991). However, 3D model (Figure 6c,d) demarcates the anomaly 1.5 km north of the fault marked (Figure 1; Majumdar et al. (2000)). We therefore infer that the deeper conductive part of the fault is offset by  $\sim 1.5$  km to the north of its surface trace or that the fault is not conductive at all but juxtaposes formations with different electrical properties. The fault itself in such a scenario would need to be listric to explain the observed offset between surface trace and deeper roots. Another possible explanation is that the fault juxtaposes different formations of rock types, one of which is dense, sealed and/or with low porosities and permeabilities, the other more porous and/or consisting from fractures

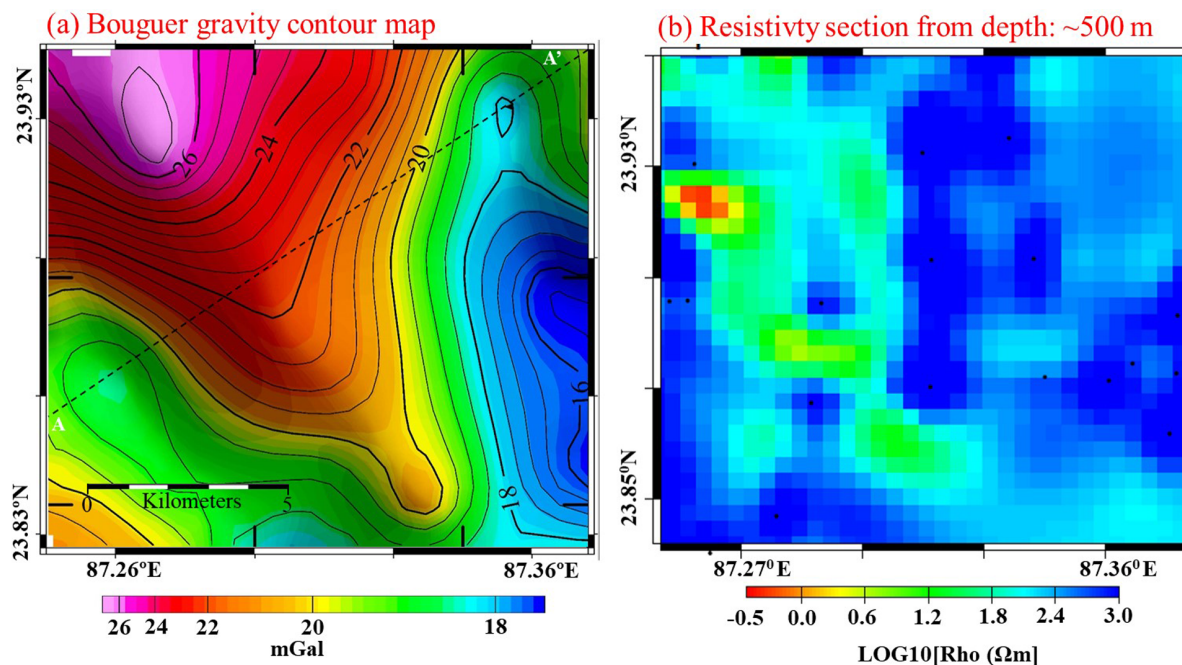


**FIGURE 10** (a) Bouguer gravity contour map redrawn after Sinharay (2006) with contours from 15 to 27 mGal. (b) Resistivity horizontal section at depth of ( $\sim 500$  m) of the 3D model (Figure 6). AA' in (a) presents the profile along which two-layered gravity modelling has been performed (Figure 13).

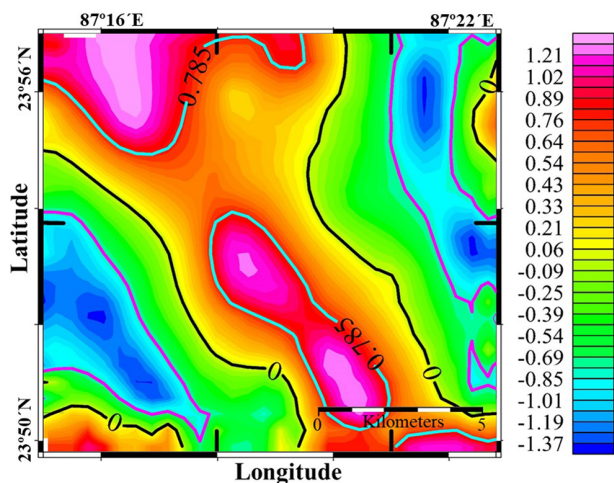


**FIGURE 11** Tilt angle derivative map of the Bouguer gravity data (Figure 10a). The black, cyan and magenta lines represent the 0, the +0.785 and -0.785 radian contours of the tilt angle, respectively.

possessing high permeabilities. Such structures could then serve as fluid conduits or reservoirs. The anomaly C2 shallows towards the eastern end and most likely merges with conductivity anomaly C1. The position of C2 also coincides to the  $0^\circ$  radian contour at the SW end of the TDR map at a depth of  $\sim 2.5$  km (Figure 12b). As the  $0^\circ$  radian contour also represents the boundary of the gravity causative source, it may suggest that C2 may represent the boundary of the Oil and Natural Gas Corporation fault, and this boundary acts

as conduit path for the geothermal fluid. Unlike C1, forward modelling was not performed for C2 due to limited coverage of the gravity data. Different models obtained from different inversion procedures have always suggested the existence of this connection, but for a more detailed and accurate mapping, we would need a better site coverage to the south of the BHS. This anomaly might also represent the northern boundary fault of the intra-cratonic Gondwana sedimentaries. These Gondwana sedimentaries are a part of Damodar Valley group of Gondwana depocentres. The offset between the boundary fault and the Gondwana sedimentaries (Figure 1) shows that the boundary faults controlling the sedimentation are generally en-echelon in nature and are sub-parallel to the Precambrian tectonic grain of Chotanagpur Granite Gneissic Complex (CGGC) (Ghosh et al., 1993). These en echelon faults are important in understanding the overall deformation and evolution of tectonic plate boundaries, and therefore, several surface/subsurface faults are present in the region (Ghosh et al., 1993). Granitic gneisses with minor enclaves of calc-silicate, amphibolite, gabbro, pegmatite and dolerite (dykes) (Ghosh et al., 1993) with much higher resistivities are observed above C2.

### Conductive anomaly C3

When MT sites are plotted over a map provided by Ghosh et al. (1993, Figure 8), it is observed that the conductivity

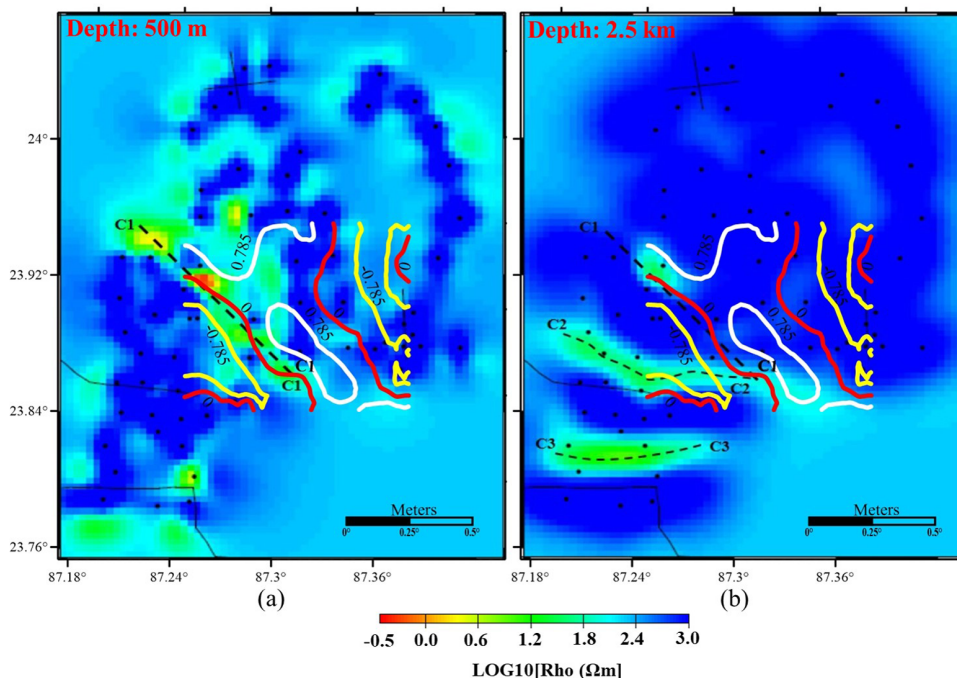


**FIGURE 12** Tilt angle derivative (TDR) contour map on top of the horizontal slice of the 3D model (Figure 8) at a depth of (a) 500 m and (b) 2.5 km. The zero-radian contour lines (red line) in the SW of the TDR map (Figure 11) are coincident with C1 and C2 of the preferred 3D magnetotelluric (MT) model (Figure 6).

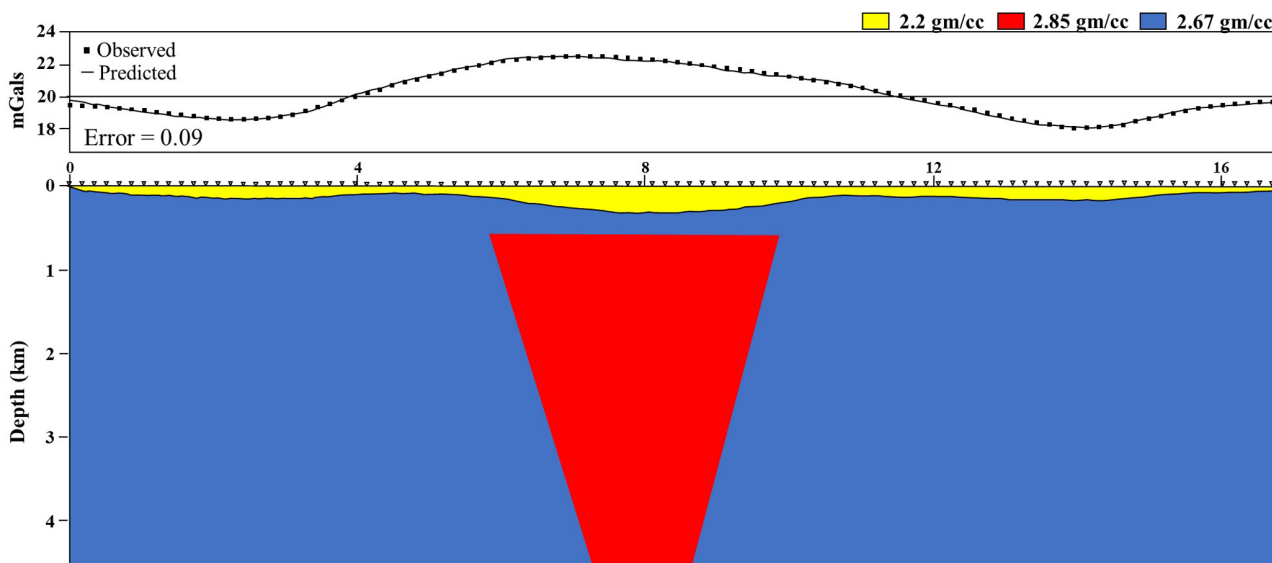


**FIGURE 13** Observed (black rectangle) and computed (black solid line) residual gravity anomaly (upper panel) and gravity model (lower panel) along same profile parallel AA' as shown in Figure 10a. The assumed average density for sediments, intrusive body and basement rocks are 2.2, 2.8 and 2.64  $\text{g/cm}^3$ , respectively. Intrusive body bisects the basement and is present from a depth of 600 m–4.5 km.

anomaly C3 is surrounded by faults and Barakar Formation or lower coal measure of Damodar valley group of the Gondwana depocentres (Ghosh et al., 1993). The Gondwana coalfields were deposited in this subsiding basin or half-grabens with basement rocks separated by faulted margins.

The contact of Gondwana rocks with the basement is marked by faulted margins, whereas the downthrown side represents a basin of deposition where a huge pile of coarse, arkosic, terrestrial and fresh water sediments were deposited (Sarolkar, 2010). These have been deposited in well-defined linear belts

of block-faulted troughs (Ghosh et al., 1993). Therefore, the interbasinal faulting and formational contacts in this region provide easy passage for the movement of subsurface water and support the conductive nature of C3.

### Conductive anomalies around Bakreswar hot spring

3D inversion model in the vicinity of the BHS (Figure 9) demarcates shallow conductive features L1, L2 and L3 of 10  $\Omega\text{m}$  at a depth slice of 0.05 km. The vertical cross-section of the model shows the presence of conducting features all along the profile, and it seems like a conductive cover layer from the cross section. These features may be due to the presence of fluids which surface out from BHS. Due to the lack of high-frequency data, NS-oriented fault (Majumdar et al., 2000) could not be delineated.

### Nature of geothermal fluid

The analysis of preferred resistivities ranging from 10 to 100  $\Omega\text{m}$  (Figure 6) as a function of salinity and temperature (Ussher et al., 2000) suggests that the fluids involved cannot be saline brines or very brackish; hinting towards the involvement of meteoric water. It also indicates that the temperatures as high as 200°C can only be observed in the region with resistivity as low as 10  $\Omega\text{m}$ . The analysis of isotopic compositions ( $\delta^{18}\text{O}$  and  $\delta\text{D}$ ) of thermal springs and local groundwater has also inferred the meteoric nature of the fluid (Majumdar et al., 2009). Moreover, Archie's law (Archie, 1942) has been used to analyse the effect of temperature and bulk resistivities on porosity. Analysis of bulk resistivity and temperature as a function of porosity (Ussher et al., 2000) suggests that the porosities in the anomalous zone are greater than 10%. Thus, it can be concluded that the fluids in our study area cannot be extremely hot throughout the entire conductivity anomaly. High conductivities in the region might either indicate a higher rate of interconnected fractures, higher salinity or higher temperatures.

### Geothermal system (heat source and the fluid path)

Bakreswar geothermal province (BGP) is a medium enthalpy and conduction-dominated geothermal system. It shows characteristics similar to conduction-dominated geothermal systems, located in or close to igneous rocks such as White Mountains in New Hampshire, Cooper Basin, Australia, northern Illinois (Roy et al., 1989) and the Gonghe basin, on the Northeastern Tibetan plateau (Zhang et al., 2020) in terms

of: (a) its location within the granites of the CGGC, (b) situated in a tectonically very stable region which has experienced no recent volcanism and (c) the source of heat is due to radiogenic process. The radiogenic process occurring in the region is supported by the high concentration of helium and very low ratios of Kr/Xe in the gas discharge from the area. The meteoric origin of water is explained by the isotopic studies performed in the region.

Anomalies C1 and C2, along with L1 and L2, represent the features which provide a possible pathway for the movement of geothermal fluid which is of meteoric origin. Based on the favourable structural settings for geothermal exploitation, BGP with anomalies C1, C2, L1 and L2 resembles to the accommodation zones (Jolie et al., 2021; Figure 4d) which is characterized by intersecting and terminating faults. Based on the current site coverage and experimental setup with frequencies higher than 10 Hz, we were only able to map a confined part of the entire geothermal system. We imaged structures probably indicating at fractured rocks that are reasonably conductive and thus could be a part of fracture system involved in the entire geothermal setting which feeds the BHS. Anomaly C3 does not play any role to the movement of geothermal fluid. Possible geo-electric model of the geothermal province is shown in Figure 14 where the anomalous structures are shown by an iso-surface resistivity value of 100  $\Omega\text{m}$ . The arrow shows the movement of meteoric water in the region.

### CONCLUSION

Bakreswar geothermal province (BGP) is a medium enthalpy geothermal system located within the granites of Chotanagpur Granite Gneissic Complex. The magnetotelluric (MT) survey was carried over a part of BGP to map the geothermal reservoir with its fluid pathways and the related geological structures. The MT model maps four prominent conducting features in the study area. Joint interpretation based on conductivity model (MT data) and density model (gravity data) suggests that the boundary of the northwest–southeast conducting feature, east–west conducting boundary fault to the south of the northwest–southeast conducting feature (which lies 1 km north of the Oil and Natural Gas Corporation fault marked by previous studies), and the conductive features located close to Bakreswar hot spring (BHS) may provide a possible pathway for fluids in the region. There is no cap-like structure observed in BGP. The favourable structural settings for BGP resemble to the accommodation zones which is characterized by intersecting and terminating faults.

Geothermal fluids that are of meteoric origin move within the region with porosities in the anomalous zone greater than 10% reaching to a maximum of 2.7 km. At this depth, the fluid comes in contact with deep-seated structures which are heated by radiogenic processes and eventually heat the

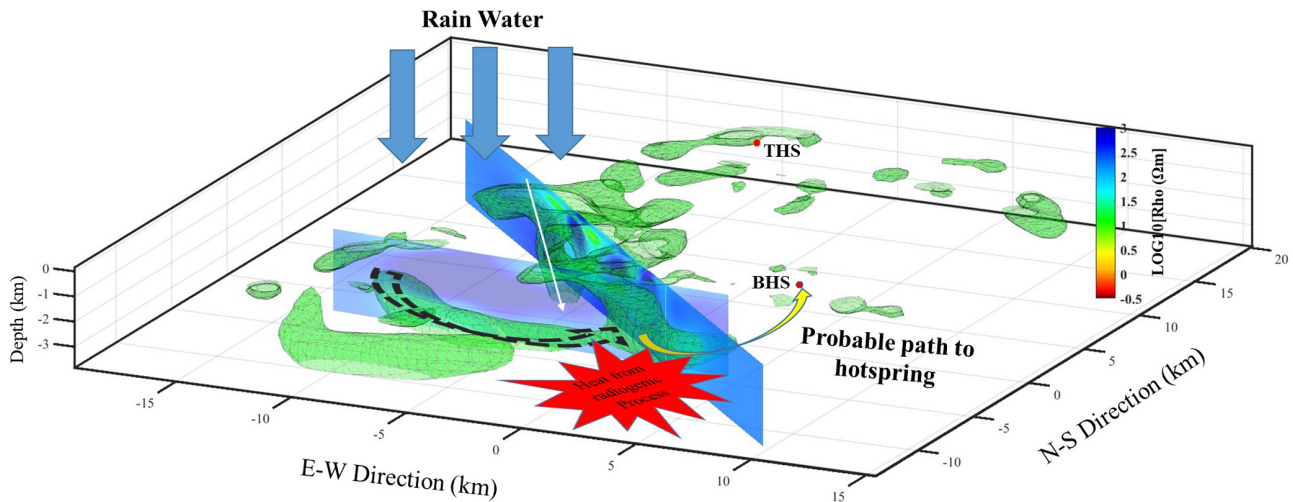


**FIGURE 14** Possible geo-electric model of Bakreswar geothermal province (BGP). The anomalous structures in the region are represented by iso-surface resistivity value of  $100 \Omega\text{m}$ . Arrows represent the movement of meteoric water. The meteoric water penetrates deep into the Earth gets heated from the radiogenic process shown by the 'red star' and rises up and comes out through the Bakreswar hot spring (BHS). The yellow arrow shows the probable path of the meteoric water but due to lack of magnetotelluric (MT) sites in the region it cannot be established.

surrounding water; this could later reach the surface close to the BHS.

## ACKNOWLEDGEMENTS

RS would like to acknowledge the Deutscher Akademischer Austauschdienst (DAAD) for providing the necessary funds for carrying out this work. We would also like to thank Dr. Naser Meqbel for providing the 3D Grid software which helped in preparation and display of the inversion data and results. RS would like to thank the German Research Centre for Geosciences (GFZ), Potsdam for providing the necessary infrastructure to carry out this work. RS thanks Ansuman Bakshi, Geological Survey of India and Dr. Avinash Chouhan, Institute of Seismological Research, Gujarat for their valuable comments on the interpretation of gravity data. RS is thankful to the members of field party for their contribution in data acquisition.

Open access funding enabled and organized by Projekt DEAL.

## DATA AVAILABILITY STATEMENT

The data that support the findings of this study are available from Indian Institute of Technology (ISM) Dhanbad, India. Restrictions apply to the availability of these data, which were used under license for this study. Data are available from the corresponding author at with the permission of Indian Institute of Technology (ISM), Dhanbad, India.

## ORCID

Roshan K. Singh  <https://orcid.org/0000-0003-1828-0840>

Shalivahan Srivastava  <https://orcid.org/0000-0002-3246-5289>

## REFERENCES

- Amatyakul, P., Rung-Arunwan, T. & Siripunvaraporn, W. (2015) A pilot magnetotelluric survey for geothermal exploration in Mae Chan region, northern Thailand. *Geothermics*, 55, 31–38.
- Arango, C., Marcuello, A., Ledo, J. & Queralt, P. (2009) 3D magnetotelluric characterization of the geothermal anomaly in the Lluçmajor aquifer system (Majorca, Spain). *Journal of Applied Geophysics*, 68, 479–488.
- Archie, G.E. (1942) The electrical resistivity log as an aid in determining some reservoir characteristics. *Transactions of the AIME*, 146, 54–67.
- Bai, D., Meju, M.A. & Liao, Z. (2001) Magnetotelluric images of deep crustal structure of the Rehai geothermal field near Tengchong, southern China. *Geophysical Journal International*, 147, 677–687.
- Benderitter, Y. & Cormy, G. (1990) Possible approach to geothermal research and relative cost estimate. In: Dickson, M.H. & Fanelli, M. (Eds.) *Small geothermal resources*. Rome, Italy: UNITAR/UNDP Centre for Small Energy Resources, pp. 61–71.
- Bhattacharya, R.S., Dutta, G.K. & Rao, P.R. (1992) *Report on geophysical mapping around Bakreswar–Tantloie group of hot springs, Birbhum district, West Bengal* (Unpublished report). Kolkata, India: Geological Survey of India.
- Bhattacharya, B.B., Sinharay, R.K. & Shalivahan (2002) Audiomagnetotelluric (AMT) investigations for 2D electrical conductivity modelling over geothermal province of Bakreswar, eastern India. In: *72nd Annual International Meeting, SEG* (Expanded Abstracts). Houston, TX, SEG. pp. 488–491.
- Bibby, H.M., Caldwell, T.G., Davey, F.J. & Webb, T.H. (1995) Geophysical evidence on the structure of the Taupo Volcanic Zone and its hydrothermal circulation. *Journal of Volcanology and Geothermal Research*, 68, 29–58.
- Bibby, H.M., Caldwell, T.G. & Brown, C. (2005) Determinable and non-determinable parameters of galvanic distortion in magnetotellurics. *Geophysical Journal International*, 163, 915–930.

- Birch, F., Roy, R.F. & Decker, E.R. (1968) Heat flow and thermal history in New England and New York. In: Zen, E., White, W.S., Hadley, J.B. & Thompson, J.B., Jr. (Eds.) *Studies of Appalachian geology, Northern and Maritime*. New York: Interscience, pp. 437–451.
- Booker, J.R. (2014) The magnetotelluric phase tensor: a critical review. *Surveys in Geophysics*, 35, 7–40.
- Branch, T., Ritter, O., Weckmann, U., Sachsenhofer, R.F., Schilling, F. (2007) The Whitehill Formation – a high conductivity marker horizon in the Karoo Basin. *South African Journal of Geology*, 110(2–3), 465–476.
- Cagniard, L. (1953) Basic theory of the magneto-telluric method of geophysical prospecting. *Geophysics*, 18, 605–635.
- Caldwell, T.G., Bibby, H.M. & Brown, C. (2004) The magnetotelluric phase tensor. *Geophysical Journal International*, 158, 457–469.
- Chandrasekharam, D. (2000) Geothermal energy resources of India. In: *Proceedings of World Geothermal Energy Congress, 28 May 28–June 10, Kyushu, Tohoku, Japan*. pp. 133–145.
- Chaudhuri, H., Das, N.K., Bhandari, R.K., Sen, P. & Sinha, B. (2010) Radon activity measurements around Bakreswar thermal springs. *Radiation Measurements*, 45, 143–146.
- Curewitz, D. & Karson, J.A. (1997) Structural settings of hydrothermal outflow: Fracture permeability maintained by fault propagation and interaction. *Journal of Volcanology and Geothermal Research*, 79, 149–168.
- Deb, S. & Mukherjee, A.L. (1969) On the genesis of a few groups of thermal springs in the Chotanagpur Gneissic Complex. *Journal of the Geological Society of India*, 4, 1–9.
- Desikachar, S.V. (1974) Himalayan orogeny and plate tectonics—A geological interpretation. In: *Miscellaneous publication – Geological Survey of India*, vol. 34. Kolkata, India: Geological Survey of India. pp. 29–39.
- Duba, A.G. (1977) Electrical conductivity of coal and coal char. *Fuel*, 56, 441–443.
- Dunn, J.A. (1939) Post-Mesozoic movements in the northern part of the peninsular India. *Memoir of Geological Survey of India*, 73, 137–142.
- Dunn, J.A. (1941) Mineral resources of Bihar. *Memoir of Geological Survey of India*, 78.
- Egbert, G.D. & Kelbert, A. (2012) Computational recipes for electromagnetic inverse problems. *Geophysical Journal International*, 189, 251–267.
- Fairhead, J.D., Salem, A., Williams, S. & Samson, E. (2008) Magnetic interpretation made easy: the tilt-depth-dip- $\Delta k$  method. In *SEG technical program expanded abstracts*. Houston, TX: SEG. pp. 779–783.
- Faulds, J.E. & Stewart, J.H. (Eds.) (1998) *Accommodation zones and transfer zones; the regional segmentation of the Basin and Range Province*, vol. 323. Boulder, CO: Geological Society of America.
- Faulds, J.E., Hinz, N.H., Dering, G.M. & Drew, D.L. (2013) The hybrid model – the most accommodating structural setting for geothermal power generation in the Great Basin, Western USA. *Geothermal Resources Council—Transactions*, 37, 3–10.
- Ghosh, P.K. (1948) Mineral springs of India. In: *Proceeding of 35th Indian Science Congress, Part 2*. Kolkata, India: Indian Science Congress. pp. 221–250.
- Ghosh, D., Das, L.K., Ghatak, T.K., Saha, D.K. & Bose, R.N. (1993) Morphotectonic configuration of cratonic Gondwana depocentres of eastern India. *Tectonophysics*, 223, 423–438.
- Ghose, N.C. & Chatterjee, N. (2008) Petrology, tectonic setting and source of dykes and related magmatic bodies in the Chotanagpur Gneissic Complex, eastern India. In: *Indian dykes: geochemistry, geophysics and geochronology*. New Delhi, India: Narosa Publishing House Pvt Ltd, pp. 471–493.
- Goldstein, B.A., Hiriart, G., Tester, J.W., Bertani, R., Bromley, C.J., Gutierrez-Negrin, et al. (2011) Great expectations for geothermal energy to 2100. In: *Proceedings of the 36th Workshop of Geothermal Reservoir Engineering, 31 January–2 February 2011, Stanford University, Stanford, CA (SGP-TR-191)*. Stanford, CA: Stanford University. pp. 5–12.
- GSI (Geological Survey of India). (1991) *Geothermal atlas of India (Special publication)*. Kolkata, India: Geological Survey of India.
- Gupta, M.L., Narain, H. & Saxena, V.K. (1976) Geochemistry of thermal waters from various geothermal provinces of India. In: *International Association of Hydrological Sciences Proceedings of the Grenoble Symposium*. Wallingford, Oxfordshire, UK: International Association of Hydrological Sciences. pp. 47–58.
- Gupta, R.K., Gupta, T., Das, R., Maji, C. & Chaudhuri, H. (2015) Geothermal potential of Bakreswar–Tantloi geothermal area, West Bengal–Jharkhand: a promising green energy resource. In: *India International Science Festival-2015 (International Conference)*, New Delhi, India.
- Hacıoğlu, Ö., Başoğur, A.T., Diner, Ç., Meqbel, N., Arslan, H.İ. & Oğuz, K. (2020) The effect of active extensional tectonics on the structural controls and heat transport mechanism in the Menderes Massif geothermal province: inferred from three-dimensional electrical resistivity structure of the Kurşunlu geothermal field (Gediz Graben, western Anatolia). *Geothermics*, 85, 101708. <https://doi.org/10.1016/j.geothermics.2019.07.006>
- Harinarayana, T., Azeed, K.A., Murthy, D.N., Veeraswamy, K., Rao, S.E., Manoj, C. & Naganjaneyulu, K. (2006) Exploration of geothermal structure in Puga geothermal field, Ladakh Himalayas, India by magnetotelluric studies. *Journal of Applied Geophysics*, 58, 280–295.
- Heise, W., Ogawa, Y., Bertrand, E.A., Caldwell, T.G., Yoshimura, R., Ichihara, H. et al. (2019) Electrical resistivity imaging of the inter-plate coupling transition at the Hikurangi subduction margin, New Zealand. *Earth and Planetary Science Letters*, 524, 115710.
- Hersir, G.P., Árnason, K. & Vilhjálmsson, A.M. (2013) 3D inversion of magnetotelluric (MT) resistivity data from Krýsuvík high temperature geothermal area in SW Iceland. In: *38th Workshop on Geothermal Reservoir Engineering, 11–13 February 2013 (SGP-TR-198)*. Stanford, CA: Stanford University.
- Hill, G.J., Caldwell, T.G., Heise, W., Chertkoff, D.G., Bibby, H.M., Burgess, M.K. et al. (2009) Distribution of melt beneath Mount St Helens and Mount Adams inferred from magnetotelluric data. *Nature Geoscience*, 2, 785–789.
- Jacobsen, B.H. (1987) A case for upward continuation as a standard separation filter for potential-field maps. *Geophysics*, 52, 1138–1148.
- Jolie, E., Scott, S., Faulds, J., Chambefort, I., Axelsson, G., Gutiérrez-Negrín, L.C., Regenspurg, S., Ziegler, M., Ayling, B., Richter, A. & Zemedkun, M.T. (2021) Geological controls on geothermal resources for power generation. *Nature Reviews Earth & Environment*, 2, 324–339.
- Kelbert, A., Meqbel, N., Egbert, G.D. & Tandon, K. (2014) ModEM: a modular system for inversion of electromagnetic geophysical data. *Computers & Geosciences*, 66, 40–53.
- Kumar, A. & Ahmad, T. (2007) Geochemistry of mafic dykes in part of Chotanagpur Gneissic Complex: petrogenetic and tectonic implications. *Geochemical Journal*, 41, 173–186.
- Majumdar, R.K., Majumdar, N. & Mukherjee, A.L. (2000) Geoelectric investigations in Bakreswar geothermal area, West Bengal, India. *Journal of Applied Geophysics*, 45, 187–202.

- Majumdar, N., Majumdar, R.K., Mukherjee, A.L., Bhattacharya, S.K. & Jani, R.A. (2005) Seasonal variations in the isotopes of oxygen and hydrogen in geothermal waters from Bakreswar and Tantloi, Eastern India: implications for groundwater characterization. *Journal of Asian Earth Sciences*, 25, 269–278.
- Majumdar, N., Mukherjee, A.L. & Majumdar, R.K. (2009) Mixing hydrology and chemical equilibria in Bakreswar geothermal area, eastern India. *Journal of Volcanology and Geothermal Research*, 183, 201–212.
- Martí, A. (2014) The role of electrical anisotropy in magnetotelluric responses: from modelling and dimensionality analysis to inversion and interpretation. *Surveys in Geophysics*, 35, 179–218.
- Meju, M.A. (2002) Geoelectromagnetic exploration for natural resources: models, case studies and challenges. *Surveys in Geophysics*, 23, 133–206.
- Meqbel, N. (2009) *The electrical conductivity structure of the Dead Sea Basin derived from 2D and 3D inversion of magnetotelluric data* (Ph.D. thesis, dissertation). Berlin, Germany: Freie Universität.
- Meqbel, N.M., Egbert, G.D., Wannamaker, P.E., Kelbert, A. & Schultz, A. (2014) Deep electrical resistivity structure of the northwestern US derived from 3-D inversion of USArray magnetotelluric data. *Earth and Planetary Science Letters*, 402, 290–304.
- Miller, H.G. & Singh, V. (1994) Potential field tilt—a new concept for location of potential field sources. *Journal of Applied Geophysics*, 32, 213–217.
- Moeck, I.S. (2014) Catalog of geothermal play types based on geologic controls. *Renewable and Sustainable Energy Reviews*, 37, 867–882.
- Mukhopadhyay, D.K. (1996) Geothermal parameters and thermal energy potential of Bakreswar, Tantloi group of hot springs in Birbhum district, West Bengal and Dumka district, Bihar. Proc. Sem. on Geothermal Energy in India. In: Pitale, U.L., Padhi, R.N.
- Mukhopadhyay, D.K. (1989) *Interim report on Bakreshwar, Tantloi and adjoining hot springs in parts of Birbhum district, WB and Dumka, Godda and Sahebganj district, Bihar* (unpublished report FS). Kolkata, India: Geological Survey of India (eastern region), pp. 88–89.
- Muñoz, G., Ritter, O. & Moeck, I. (2010) A target-oriented magnetotelluric inversion approach for characterizing the low enthalpy Groß Schönebeck geothermal reservoir. *Geophysical Journal International*, 183, 1199–1215.
- Munoz, G. (2014) Exploring for geothermal resources with electromagnetic methods. *Surveys in Geophysics*, 35, 101–122.
- Nagar, R.K. (1996) Geological, geophysical and geochemical investigations in Bakreswar–Tantloi thermal field, Birbhum and Santhal Parganas districts, West Bengal and Bihar, India, Geothermal Energy in India (special publication) vol. 45. Kolkata, India: Geological Survey of India. pp. 349–360.
- Neuendorf, K.E., Mehl, J.P., Jr. & Jackson, J.A. (2005) Glossary of Geology. 5th ed. Alexandria VA: American Geosciences Institute.
- Noller, N.M.W. & Daly, J.S., the IRETherm Team. (2015) The contribution of radiogenic heat production studies to hot dry rock geothermal resource exploration in Ireland. In: Proceedings World Geothermal Congress.
- ONGC. (1969) *Tectonic map of India* (scale 1:20000). Dehradun, India: Oil and Natural Gas Commission.
- Oskooi, B., Pedersen, L.B., Smirnov, M., Árnason, K., Eysteinnsson, H., Manzella, A. & Working Group, D.G.P. (2005) The deep geothermal structure of the Mid-Atlantic Ridge deduced from MT data in SW Iceland. *Physics of the Earth and Planetary Interiors*, 150, 183–195.
- Patro, P.K. (2017) Magnetotelluric studies for hydrocarbon and geothermal resources: examples from the Asian region. *Surveys in Geophysics*, 38, 1005–1041.
- Platz, A. & Weckmann, U. (2019) An automated new pre-selection tool for noisy Magnetotelluric data using the Mahalanobis distance and magnetic field constraints. *Geophysical Journal International*, 218, 1853–1872.
- Razdan, P.N., Agarwal, R.K. & Singh, R. (2008) Geothermal energy resources and its potential in India. *Earth Science India*, 1, 30–42.
- Ritter, O., Junge, A. & Dawes, G.J. (1998) New equipment and processing for magnetotelluric remote reference observations. *Geophysical Journal International*, 132, 535–548.
- Ritter, O., Klose, R. & Weckmann, U. (2015) EMERALD data format for magnetotelluric data (Scientific technical report—data; 15/08). Potsdam: Deutsches GeoForschungsZentrum GFZ. <https://doi.org/10.2312/GFZ.b103-15082>
- Roche, V., Bouchot, V., Beccalotto, L., Jolivet, L., Guillou-Frottier, L., Tuduri, J., Bozkurt, E., Oğuz, K., Tokay, B. (2019) Structural, lithological and geodynamic controls on geothermal activity in the Menderes geothermal province (Western Anatolia, Turkey). *International Journal of Earth Sciences*, 108, 301–328. <https://doi.org/10.1007/s00531-0181655-1>
- Rowland, J.V. & Simmons, S.F. (2012) Hydrologic, magmatic, and tectonic controls on hydrothermal flow, Taupo Volcanic Zone, New Zealand: implications for the formation of epithermal vein deposits. *Economic Geology*, 107, 427–457.
- Roy, A.K., Bagchi, A., Chatterjee, P., Mukherjee, A. & Brahman, C.V. (1985) *Reconnaissance geophysical investigation for locating source of geothermal energy in Bakreswar area, Birbhum district, West Bengal* (Un-published report). Kolkata, India: Geological Survey of India.
- Roy, R.F., Rahman, J.L. & Blackwell, D.D. (1989) Heat flow at UPH-3, northern Illinois (abst.). *EOS*, 70, 1321.
- Saada, S.A. (2016) Edge detection and depth estimation of Galala El Bahariya Plateau, Eastern Desert-Egypt, from aeromagnetic data. *Geomechanics and Geophysics for Geo-Energy and Geo-Resources*, 2, 25–41.
- Salem, A., Williams, S., Fairhead, J.D., Ravat, D. & Smith, R.S. (2007) Tilt-depth method: a simple depth estimation method using first-order magnetic derivatives. *The Leading Edge*, 26, 1502–1505.
- Salem, A., Williams, S., Fairhead, J.D., Smith, R.S. & Ravat, D. (2008) Interpretation of magnetic data using tilt-angle derivatives. *Geophysics*, 73, L1–L10.
- Sarang, A.K. (2003) Grade control in Jaduguda uranium mine, Jharkhand. *The Transactions, the Mining Geological and Metallurgical institute of India*, 99, 1–2.
- Sarkar, A.N. (1982) Precambrian tectonic evolution of eastern India: a model of converging microplates. *Tectonophysics*, 86, 363–397.
- Sarolkar, P. (2010) Exploration strategy for hot springs associated with Gondwana coalfields in India. *Proceedings World Geothermal Congress*, 74, 68.
- Sarolkar, P.B. (2018) Geothermal energy in India: poised for development. In: *Proceedings of 43rd Workshop on Geothermal Reservoir Engineering, 12–14 Feb. 2018, Stanford University, Stanford, CA* (SGP-TR-213). Stanford, CA: Stanford University.
- Shanker, R. (1988) Heat flow map of India and discussion on its geological and economic significance. *Indian Minerals*, 42, 89–110.

- Shanker, R. (1991) Thermal and crustal structure of "SONATA". A zone of mid continental rifting in Indian Shield. *Journal of the Geological Society of India*, 37, 211–220.
- Simpson, F. & Bahr, K. (2005) *Practical magnetotellurics*. Cambridge, United Kingdom: Cambridge University Press.
- Singh, H.K., Chandrasekharam, D., Vaselli, O., Trupti, G., Singh, B., Lashin, A. & Al Arifi, N. (2015) Physico-chemical characteristics of Jharkhand and West Bengal thermal springs along SONATA mega lineament, India. *Journal of Earth System Science*, 124, 419–430.
- Singh, H.K., Chandrasekharam, D., Trupti, G., Mohite, P., Singh, B., Varun, C. & Sinha, S.K. (2016) Potential geothermal energy resources of India: a review. *Current Sustainable/Renewable Energy Reports*, 3(3–4), 80–91.
- Singh, R.K., Maurya, V.P., Shalivahan & Singh, S. (2019) Imaging regional geology and Au–sulphide mineralization over Dhanjori greenstone belt: implications from 3-D inversion of audio magnetotelluric data and petrophysical characterization. *Ore Geology Reviews*, 106, 369–386.
- Sinharay, R.K. (2006) *Application of magnetotelluric (MT) method for the study of geothermal resources in Bakreswar, Eastern India* (Ph.D. thesis). India: Indian School of Mines.
- Sinharay, R.K., Srivastava, S. & Bhattacharya, B.B. (2010) Audio-magnetotelluric studies to trace the hydrological system of thermal fluid flow of Bakreswar Hot Spring, Eastern India: a case history. *Geophysics*, 75, B187–B195.
- Sun, Z., Wang, A., Liu, J., Hu, B. & Chen, G. (2015) Radiogenic heat production of granites and potential for hot dry rock geothermal resource in Guangdong Province, Southern China. In: *World Geothermal Congress*, 19–25 April 2015, Melbourne, Australia. pp. 2–6.
- Talwani, M., Worzel, J.L. & Landisman, M. (1959) Rapid gravity computations for two-dimensional bodies with application to the Mendocino submarine fracture zone. *Journal of Geophysical Research*, 64, 49–59.
- Talwani, M. & Heirzler, J.R. (1964) Computation of magnetic anomalies caused by two-dimensional bodies of arbitrary shape. In: *Computers in the mineral industry*. Stanford, CA: School of Earth Sciences, Stanford University.
- Telford, W.M., Telford, W.M., Geldart, L.P., & Sheriff, R.E. (1990) *Applied geophysics*. Cambridge: Cambridge University Press.
- Tester, J.W., Drake, E.M., Golay, M.W., Driscoll, M.J. & Peters, W.A. (2005) *Sustainable energy – Choosing among options*. Cambridge, MA, USA: MIT Press.
- Tikhonov, A.N. (1950) The determination of the electrical properties of deep layers of the Earth's crust. *Doklady Akademii Nauk SSR*, 73, 295–297.
- Uchida, T., Song, T., Lee, T.J., Mitsuhashi, Y., Lee, S.K. & Lim, S.K. (2004) 3D magnetotelluric interpretation in Pohang low-enthalpy geothermal area, Korea. In: *Proceedings 17th Electromagnetic Induction Workshop, Hyderabad, India*.
- Uchida, T. (2005) Three-dimensional magnetotelluric investigation in geothermal fields in Japan and Indonesia. In: *Proceedings World Geothermal Congress, Antalya, Turkey*.
- Ussher, G., Harvey, C., Johnstone, R. & Anderson, E. (2000) Understanding the resistivities observed in geothermal systems. In: *Proceedings World Geothermal Congress, Japan, 1915–1920*.
- Volpi, G., Manzella, A. & Fiordelisi, A. (2003) Investigation of geothermal structures by magnetotellurics (MT): an example from the Mt. Amiata area, Italy. *Geothermics*, 32, 131–145.
- Vozoff, K. (1972) The magnetotelluric method in the exploration of sedimentary basins. *Geophysics*, 37, 98–141.
- Wannamaker, P.E., Rose, P.E., Doerner, W.M., Berard, B.C., McCulloch, J. & Nurse, K. (2004) Magnetotelluric surveying and monitoring at the Coso geothermal area, California, in support of the enhanced geothermal systems concept: survey parameters and initial results. In: *Proceedings of the Twenty-Ninth Workshop on Geothermal Reservoir Engineering*, Stanford, CA, Stanford University. pp. 287–294.
- Weaver, J.T., Agarwal, A.K. & Lilley, F.E.M. (2000) Characterization of the magnetotelluric tensor in terms of its invariants. *Geophysical Journal International*, 141, 321–336.
- Weckmann, U., Magunia, A. & Ritter, O. (2005) Effective noise separation for magnetotelluric single site data processing using a frequency domain selection scheme. *Geophysical Journal International*, 161, 635–652.
- Wiese, H. (1962) Geomagnetische Tiefentellurik Teil II: die Streichrichtung der Untergrundstrukturen des elektrischen Widerstandes, erschlossen aus geomagnetischen Variationen. *Geofisica Pura e Applicata*, 52, 83–103.
- Williams, C.F., Reed, M.J. & Anderson, A.F. (2011) January, Updating the classification of geothermal resources. In: *Proceedings 36th workshop on geothermal reservoir engineering*. Stanford, CA, Stanford University, SGP-TR-191.
- Won, I. & Bevis, M. (1987) Computing the gravitational and magnetic anomalies due to a polygon: algorithms and Fortran subroutines. *Geophysics*, 52, 232–238.
- Xiao, Q., Cai, X., Xu, X., Liang, G. & Zhang, B. (2010) Application of the 3D magnetotelluric inversion code in a geologically complex area. *Geophysical Prospecting*, 58, 1177–1192.
- Zhang, C., Hu, S., Zhang, S., Li, S., Zhang, L., Kong, Y., Zuo, Y., Song, R., Jiang, G. & Wang, Z. (2020) Radiogenic heat production variations in the Gonghe basin, northeastern Tibetan Plateau: implications for the origin of high-temperature geothermal resources. *Renewable Energy*, 148, 284–297.

## SUPPORTING INFORMATION

Additional supporting information can be found online in the Supporting Information section at the end of this article.

**How to cite this article:** Singh, R.K., Weckmann, U. & Srivastava, S. (2024) Magnetotelluric images of the medium enthalpy Bakreswar geothermal province within a granitic gneissic complex, Eastern Indian Peninsula. *Geophysical Prospecting*, 72, 857–881. <https://doi.org/10.1111/1365-2478.13439>

## APPENDIX A

Sounding curves showing the misfit between observed and predicted 3D data for all the 65 sites used in the regional study and corresponds to 3D model (Figure 6).

See Figure A.1a–c.

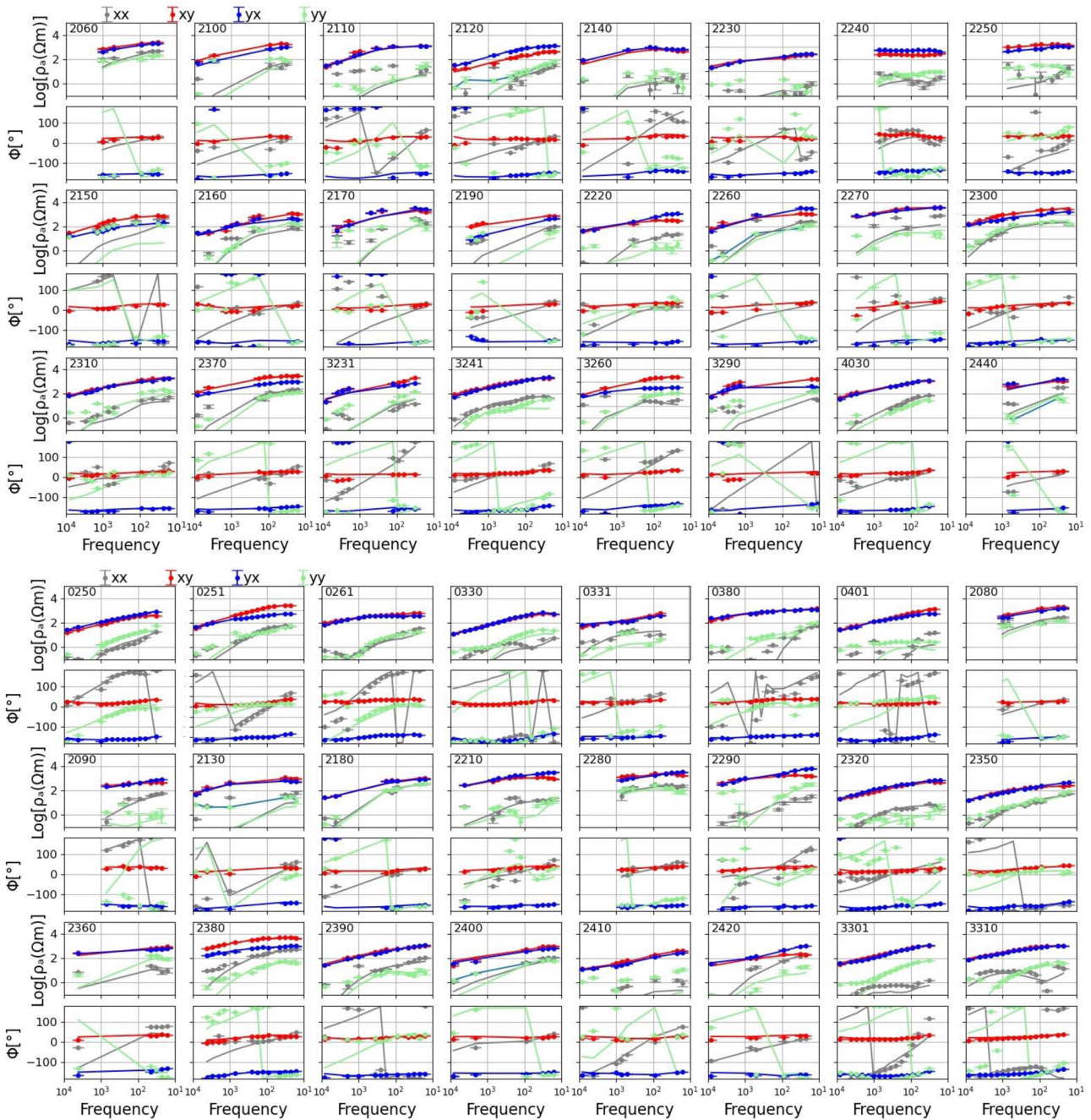


**FIGURE A.1** (a) Observed (open circles) and predicted (continuous line) data for the sites (inset in figure) used in the regional study and corresponds to 3D model (Figure 6). (b) Observed (open circles) and predicted (continuous line) data for the sites (inset in figure) used in the regional study and corresponds to 3D model (Figure 6). (c) Observed (open circles) and predicted (continuous line) data for the sites (inset in figure) used in the regional study and corresponds to 3D model (Figure 6).

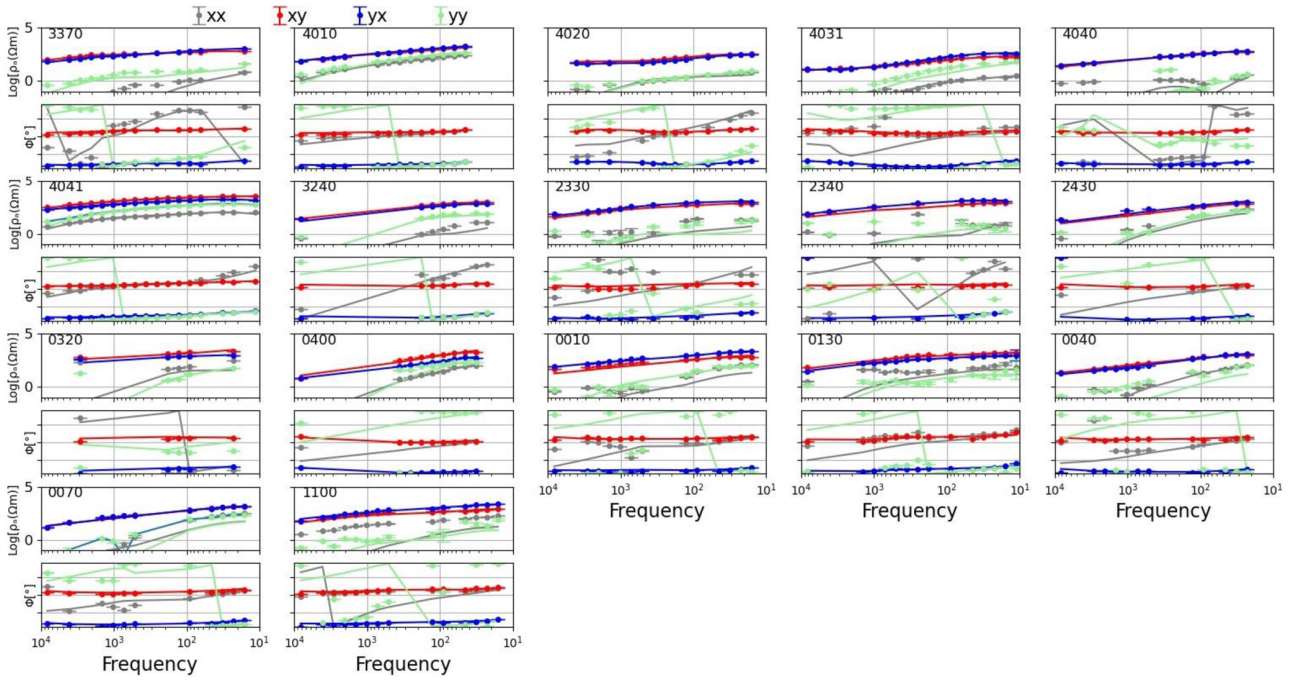


FIGURE A.1 Continued

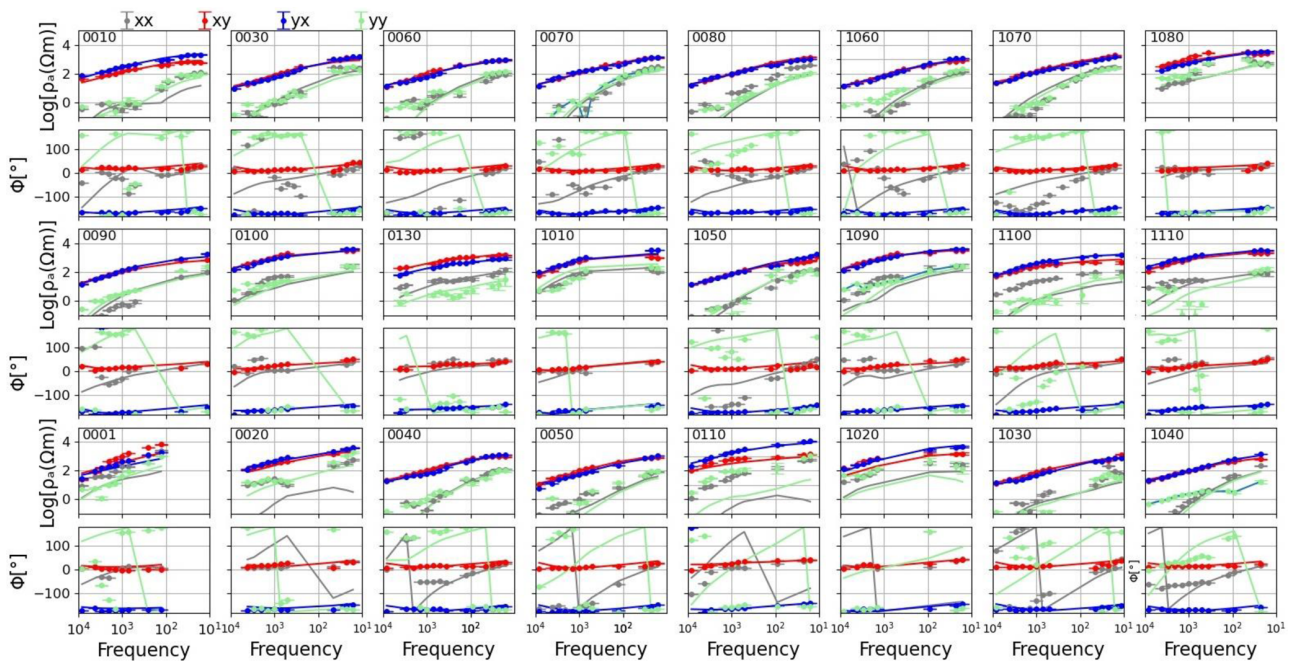


FIGURE B.1 Observed (open circles) and predicted (continuous line) 3D data for sites (inset in the figure) used in the localized study around Bakreswar hot spring (BHS) and corresponds to 3D model (Figure 9).

APPENDIX B

Sounding curves showing the misfit between observed and predicted 3D data for all the 24 sites used in the localized

study around BHS and corresponds to 3D model (Figure 9).

See Figure B.1.

APPENDIX C

See Figure C.1.

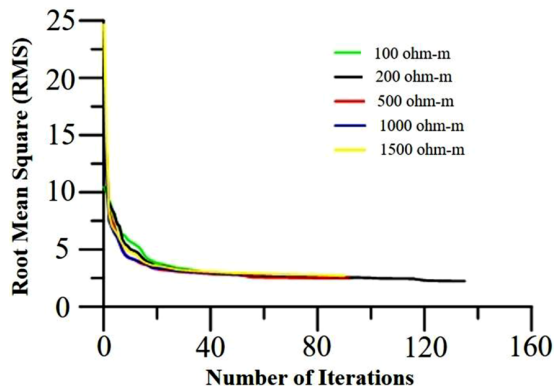


**FIGURE C.1** Convergence graph showing the overall RMS as a function of the number of iterations for the 3D inversion of impedances using an initial half space resistivity of 100 (green line), 200 (black line), 500 (red line), 1000 (blue line) and 1500  $\Omega\text{m}$  (yellow line).

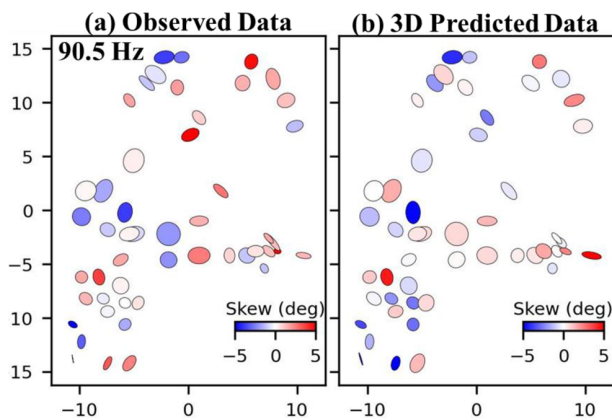


**FIGURE D.1** Map view of phase tensor ellipses coloured by skew angles ( $\beta$ ) at frequencies of 90.5 Hz for (a) observed and (b) 3D predicted data.

## APPENDIX D

See Figure D.1.

## APPENDIX E

Geological map of Bakreswar Geothermal Province showing the distribution of magnetotelluric (MT) sites used in the

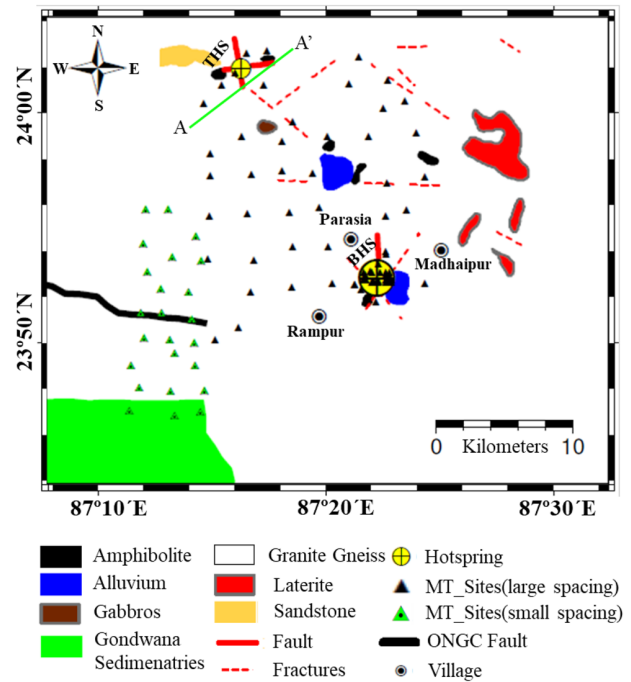


**FIGURE E.1** Geological map of the study area with the distribution of the magnetotelluric (MT) sites (black filled triangles). Black solid lines: deep-seated faults (Majumdar et al., 2000; ONGC, 1969); yellow circles: Bakreswar (BHS) and Tantloie (THS) hot springs; green dashed lines AA' represent the profile for which a vertical cross-section close to THS (Figure E.2) has been extracted. All the geological features have been plotted over the background of Chotanagpur Granite Gneissic Complex (CGGC).

study has been shown in Figure E.1. All the geological features have been plotted over the background of Chotanagpur Granite Gneissic Complex (CGGC). The map also shows the location of vertical sections AA' (green colour) along which the 3D model (Figure 6) has been extracted to show the model features around Tantloie hot spring (THS) (Figure E.2).

The vertical cross-section close to the THS (Figure E.2) indicates lower resistivities between sites 2090 and 2390. This anomalous feature is quite shallow and can be observed to a depth of  $\sim 1.5$  km.

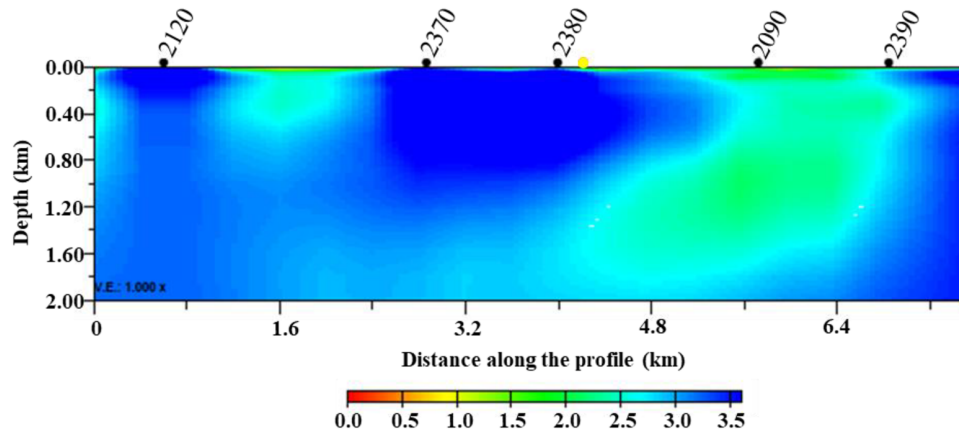


**FIGURE E.2** Vertical cross section (profile AA' in Figure E.1) of the final 3D model close to the Tantloie hot spring (THS). The yellow circle marks the surface expression of the THS.